Response to Referee#1

Thank you for your careful assessment and valuable comments. The comments and suggestions are very useful for our manuscript. We have carefully studied these comments and suggestions and made some changes in our manuscript.

Comment 1)

"To overcome these limitations" … I think especially the sensitivity to Mie scattering is not solved yet. Your temperature profiles can only be used above 5.3 km due to the contamination from aerosols. Hence, I would skip this argument in the abstract.

Response:

Thank you for this important comment. We agree that the influence of Mie scattering is not completely eliminated and that the original wording was not sufficiently precise. Following the reviewer's suggestion, we have revised the manuscript accordingly. These revisions have been made in the Abstract on Page 1, Lines 13–18 and 24–26, and Page 2, Lines 54–62.

Comment 2)

As you are addressing RB scattering research, which I think is indeed very crucial for the presented measurement technology, it might be useful to mention the first studies performed in air: https://doi.org/10.1364/AO.49.004217

Response:

Thank you for this helpful suggestion. We have added the pioneering experimental study by Witschas et al. (2010) to the Introduction when discussing early Rayleigh–Brillouin scattering measurements in air. The corresponding reference and a brief description of its contribution have been added on Page 2–3, Lines 62–64.

Comment 3)

You approximate the Fizeau transmission function, which is only a valid approach for low-Finesse systems. For high-Finesse Fizeau interferometers, a clearly asymmetric

transmission function arises, which has to be considered. I would recommend justifying your approach here.

Response:

Thank you for this valuable comment. We agree that the applicability of the Airy-function approximation should be further justified. Following McKay (Mckay, 2002), we have introduced the shape factor S and its calculation in the revised manuscript. For the developed Fizeau interferometer, the calculated shape factor is S=0.062. This value is well below the criterion of S<0.6, supporting the applicability of the Airy-function approximation to the interference fringe. The relevant definitions, calculation, reference, and discussion have been added to Page 5, Lines 136-143 while the calculated value of S and the corresponding conclusion have been added to Page 11, Lines 266–267 of the revised manuscript.

Comment 4)

In the Rayleigh-Brillouin community, your parameters "a" and "b" are usually called the dimensionless frequency "x" and the parameter "y." I think you could either use this nomenclature or, at least, briefly mention it here.

Response:

Thank you for this comment. We have revised the corresponding variables to x and y and clarified their definitions on Page 6, Lines 154-169.

Comment 5)

I think it is better to call θ the scattering angle. It would also be useful to give numbers for the shear viscosity in air (the value that you use) and for θ = 180° for lidar measurements.

Response:

Thank you for this comment. We have replaced "divergence angle" with "scattering angle" and clarified that $\theta = 180°$ for lidar backscattering measurements on Page 6, Lines 164. We have also specified the shear viscosity of air used in the calculation, $\eta = 1.846 \times 10^{-5}\ \mathrm{kg\,m^{-1}\,s^{-1}}$, which is used in the calculation of the uniformity

parameter y in the G3 model(Witschas, 2011a, b; Witschas et al., 2010), on Page 6, Line 162.

Comment 6)

It is very important to distinguish between the correct physical line-shape model by Tenti, which has no closed analytical form, and the approximation by Witschas, which is based on the superposition of three Gaussians, as you show in Eq. (8). As Witschas derived his model based on the x and y parameters, it is indeed possible to substitute these and make it dependent on p and T. However, it has to be made clear that this is the equation by Witschas and not the Tenti model.

Response:

Thank you for this important comment. We have clarified that the Tenti S6 model has no closed-form analytical expression and that Eq. (9) is the three-Gaussian analytical approximation developed by Witschas (Witschas, 2011a, b). These revisions have been made on Page 6, Lines 154-169.

Comment 7)

Can you also provide numbers for the spectral pulse width as well as the frequency stability of the laser, which are both important quantities for the applied technology?

Response:

Thank you for this valuable comment. We acknowledge that the spectral linewidth of the pulsed laser was not independently measured during the experiment. According to the manufacturer's performance report, the laser linewidth is less than 1 GHz. Importantly, the receiver transmission profile was experimentally characterized using the same pulsed laser employed for the atmospheric measurements. Therefore, the measured spectral response of the receiver inherently includes the effect of the finite laser linewidth, and this effect is consequently accounted for in the subsequent spectral analysis and retrieval.

In addition, with all other receiver parameters kept unchanged, the receiver transmission profile was independently measured using a narrow-linewidth continuous-

wave laser with a linewidth of approximately 100 kHz. Because its linewidth is negligible compared with the spectral width of the receiver, this measurement provides an approximation of the intrinsic receiver transmission function. By comparing the transmission profiles measured with the continuous-wave and pulsed lasers and performing deconvolution, the spectral linewidth of the pulsed laser was estimated to be approximately 0.67 GHz, consistent with the manufacturer-specified value of less than 1 GHz.

During the atmospheric observations on 30 June 2026, the laser frequency was continuously monitored using a HighFinesse WS8-2 wavelength meter with a frequency resolution of approximately 0.1 MHz to evaluate its frequency stability. The measured frequency fluctuations over the observation period are shown in Fig. R1.

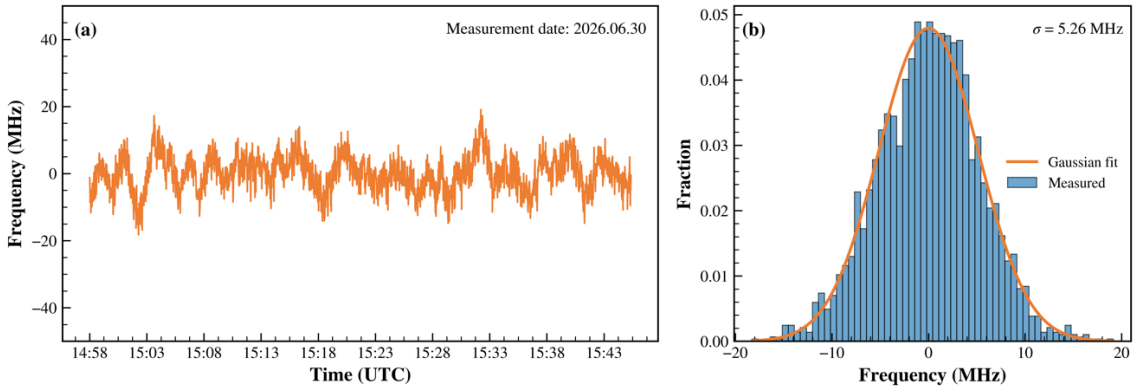


Figure R1. Laser frequency fluctuations measured by a wavelength meter during the atmospheric observation period.

The laser frequency remained stable throughout the measurement period, with a standard deviation of 5.26 MHz over the entire observation period.

Comment 8)

Using a multimode fiber should cause speckle issues in the imaged fringes. How do you deal with that? Do you use an additional fiber scrambler? Further, the larger fiber core together with the NA of 0.22 broadens the transmission fringe of the Fizeau significantly (compared to SM fiber illumination). Do you consider that? Does this cause error sources?

Response:

Thank you for this insightful comment. Yes, an additional fiber scrambler was employed after the multimode fiber to suppress speckle effects and improve the spatial uniformity of the beam incident on the Fizeau interferometer. This point has now been clarified in the revised manuscript on Page 8, Lines 189, and the fiber scrambler has also been added to the optical layout shown in Fig. 2 in manuscript to more accurately represent the actual receiver configuration.

We agree that the finite core diameter and numerical aperture (NA) of the multimode fiber introduce an angular spread in the collimated beam, which may broaden the transmission fringe of the Fizeau interferometer. In our receiver, the collected signal is coupled into a multimode fiber with a core diameter of 200 μm and an NA of 0.22. After passing through the fiber scrambler, the output beam is collimated by a lens with a diameter of 50 mm and a focal length of approximately 114 mm. The angular spread after collimation is calculated as:

$$\theta = \arctan\left(\frac{d/2}{f}\right) = \arctan\left(\frac{100\ \mu m}{114\ mm}\right) \approx 0.88\ mrad$$

The divergence half-angle is approximately 0.88 mrad. To quantitatively evaluate the influence of this finite beam divergence on the transmission characteristics of the Fizeau interferometer, the transmission profiles for divergence half-angles of 0 and 0.88 mrad were calculated using the formulation given by Born and Wolf.

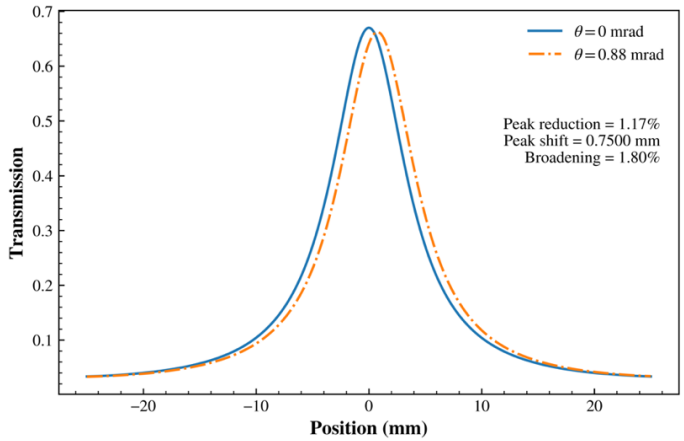


Figure R2. Effect of different divergence angles on the transmission of the Fizeau interferometer.

The calculated transmission curves for divergence half-angles of 0 and 0.88 mrad are shown in Fig. R2. Compared with the case of zero divergence, a divergence half-angle of 0.88 mrad results in only a 1.17% reduction in the peak transmission and a 1.80% increase in the full width at half maximum (FWHM), indicating that the influence of the beam divergence on the shape and width of the Fizeau transmission profile is relatively small. Meanwhile, the transmission peak is shifted by approximately 0.75 mm on the detector plane. Although these effects are limited, the finite divergence angle of the collimated beam was explicitly taken into account in our simulations.

More importantly, in the actual experiment, the receiver transmission profile was experimentally characterized using the same optical configuration as that employed for the atmospheric measurements. Therefore, the measured receiver transmission profile inherently includes the effects associated with the finite divergence angle of the incident beam, including the slight broadening and shift of the transmission fringe. Since this experimentally measured transmission profile is subsequently used in the spectral analysis and atmospheric parameter retrieval, the influence of beam divergence is already incorporated into the receiver response and thus does not introduce an additional unaccounted error in the retrieval.

Comment 9)

Why do you not use the transmission formula of a Fizeau interferometer, as for instance introduced by Born and Wolf?

Response:

Thank you for this comment. The equation used in this study is an angularly averaged Airy transmission function. The Airy function describes the basic Fizeau fringe under the small-shape-factor condition (Mckay, 2002; Vaughan et al., 2025). The integration accounts for the finite angular distribution of the incident beam, assuming a uniform circular angular distribution.

We also apologize for an omission in the original manuscript. A $\sin\theta$ term was inadvertently omitted from Eq. (10). This typographical error has now been corrected

in the revised manuscript.

To verify the validity of this approximation, we calculated the Fizeau interferometer transmission at a beam divergence half-angle of 0.88 mrad using Eq. (10) of the revised manuscript and compared it with that calculated using the Born and Wolf formulation under the same divergence condition. The comparison is presented in Fig. R3 below.

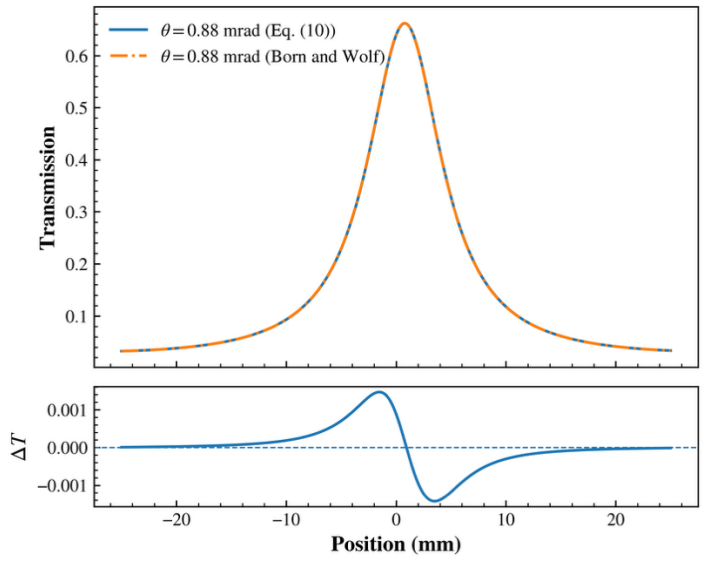


Figure R3. Comparison of the Fizeau interferometer transmission calculated using the Airy function and the Born–Wolf formulation for a divergence half-angle of 0.88 mrad.

Figure R3 compares the Fizeau transmission functions calculated using Eq. (10) and the Born and Wolf formulation at a beam divergence angle of 0.88 mrad. As shown in the upper panel, the two transmission curves almost completely overlap. The lower panel presents their difference, defined as $\Delta T = T_{Eq.\ (10)} - T_{Born\ and\ Wolf}$. The maximum absolute difference is approximately 1.5×10^{-3}, corresponding to only about 0.2% of the peak transmission. The small positive and negative residuals around the fringe peak indicate only a slight difference in fringe asymmetry and position. Therefore, Eq. (10) provides an adequate approximation to the Born and Wolf formulation under the present small-shape-factor condition.

Comment 10)

Have you performed any further numerical simulations to optimize the specifications

of the applied Fizeau interferometer? Or is this a justification that you can use an existing Fizeau interferometer for your test measurements (which would be fine, of course)?

Response:

Thank you for this comment. As explained on Page 9, Lines 205–209, the FSR of the Fizeau interferometer should be between 10 and 12.6 GHz to cover the relevant RB spectrum. An existing three-axis piezoelectrically tunable etalon with a nominal cavity spacing of 12.5 mm was used. The etalon has a free spectral range of approximately 12 GHz at the operating wavelength of 355 nm.

The etalon was initially adjusted to the parallel-plate configuration. The wedge angle required for Fizeau operation was subsequently introduced by varying only the Y-axis piezoelectric actuator, while the X- and Z-axis settings were held at their parallelism values. The differential displacement generated by the Y-axis actuator produces a relative inclination between the two etalon plates. With an effective actuator baseline of 50 mm, the wedge angle is given by:

$$\alpha = \arctan(\frac{\Delta y}{\mathrm{L}})$$

where Δy is the Y-axis displacement relative to the parallel configuration and $\mathrm{L} = 50\ \mathrm{mm}$. The parallel configuration corresponds to a Y-axis digital setting of $N_0 = 33650$. According to the manufacturer, one digital step produces a displacement of approximately 0.1–0.15 nm, and the 16-bit digital interface provides a total adjustment range of 65,535 digital steps, with the Y-axis setting varying from 0 to 65535. Starting from the parallel-plate setting of $N_0 = 33650$, the Y axis can be decreased by 33650 steps or increased by 31885 steps. Using the minimum specified displacement of 0.10 nm per step and an effective actuator baseline of 50 mm, the corresponding wedge angle can be tuned from approximately $-67.3 \sim 63.8\ \mu\mathrm{rad}$.

Therefore, the numerical simulations were not intended to redesign the Fizeau interferometer or to optimize all of its hardware specifications from first principles. Instead, we first demonstrated that the available tunable etalon had a suitable FSR and a sufficient actuator range to operate in the required Fizeau configuration. The

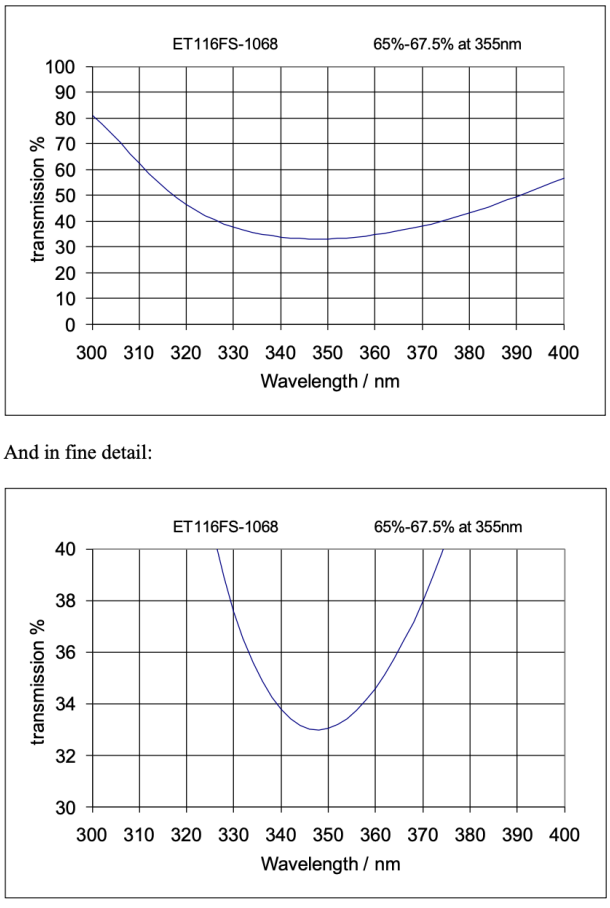
numerical simulations were then used to optimize the operating parameters of this existing device.

Comment 11)

I would expect further important specifications of the Fizeau interferometer to be mentioned here. Especially the mean plate reflectivity as well as the wedge angle that was used.

Response:

Thank you for this comment. The mean plate reflectivity (approximately 66%) at 355 nm and the wedge angle (2.83 µrad) have now been added to Table 2.



And in fine detail:

Figure R4. Measured transmission spectrum of the etalon high-reflectivity coating, with a detailed view shown on an expanded transmission scale

Comment 12)

I do not fully understand the approach or the outcome of this simulation. There is a pretty good estimation of the accuracy for the center and width determination of a Gaussian considering Poisson and white noise (Hagen et al., 2007, https://doi.org/10.1364/AO.46.005374). In this study, it is explained that one needs a certain number of channels (~3) to reach a certain accuracy. When increasing the number of channels, the accuracy does not improve, as the result of each channel gets less accurate (square root of the photons in each channel). Hence, I would expect that you do not see big differences between 32 channels and 64 or 128 channels. Of course, this also depends on the actual fringe shape that you are using, as well as on the conversion factor (channel width and corresponding imaging). I would either suggest clarifying (and checking) these points or maybe skipping this section for this paper, as it is not of primary importance.

Response:

Thank you for this insightful comment. We agree that the previous presentation did not clearly demonstrate how the number of detector channels affects the final retrieval accuracy. In the original manuscript, Fig. 3 showed the Pearson correlation coefficient between the reconstructed and simulated spectra rather than the retrieved temperature and wind errors. This coefficient is affected by both spectral sampling and the signal-to-noise ratio of the individual channels. Consequently, it did not provide a sufficiently direct measure of retrieval performance and made comparison with the expected photon-noise-limited behavior difficult.

We have therefore replaced Fig. 3 with an analysis of the root-mean-square errors (RMSEs) of the retrieved temperature and wind velocity for different detector channel numbers and altitudes, the revised Fig. 3 in manuscript is shown here as Fig. R5. The revised simulations use the same vertical resolution as the atmospheric measurements. At each altitude, the total expected detected photon count and the spectral range are held fixed across the channel configurations. The comparison therefore evaluates the effect of sampling density under the same photon budget.

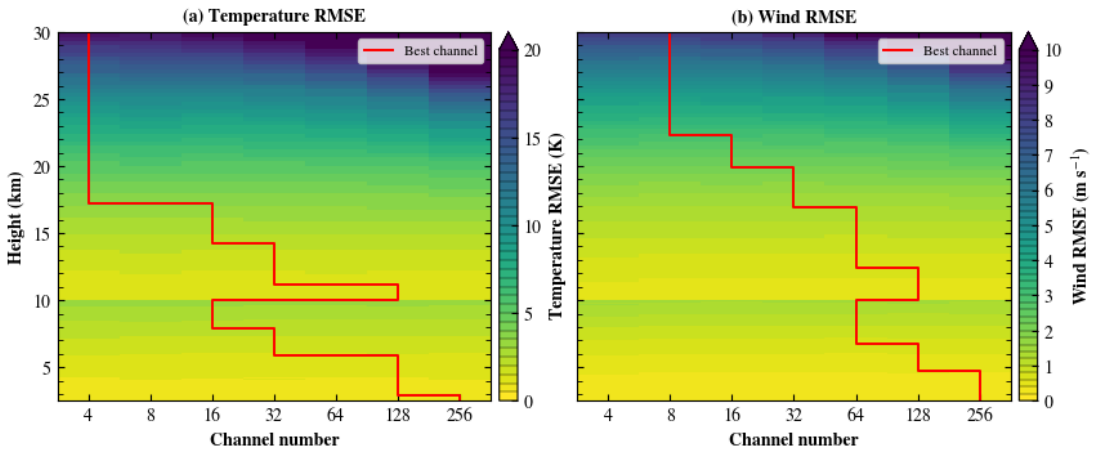


Figure R5. Influence of detector channel number and detection height on the retrieval accuracy of (a) temperature and (b) wind velocity.

Hagen et al. examined the effects of sampling density, finite pixel width, and noise on the estimation of Gaussian spectral parameters, highlighting the importance of balancing spectral sampling resolution and measurement uncertainty (Hagen et al., 2007). As shown in the Fig. R5, increasing the number of channels provides only limited improvement in retrieval accuracy, while configurations with larger numbers of channels may even exhibit degraded performance due to reduced signal-to-noise ratios (SNRs). Ultimately, the 32-channel configuration was selected as a compromise among overall system robustness, complexity, and the commercial availability of multichannel PMT arrays.

The corresponding revisions can be found on Pages 10–11, Lines 244–267.

Comment 13)

I do not understand what is shown here. Do you say that, when analyzing a simulated RB spectrum, your algorithm converges after about one iteration? This makes no sense to me. But maybe I do not understand this figure correctly.

Response:

Thank you for pointing out this ambiguity. We apologize that the definition of "iteration" was not sufficiently clear. Here, one iteration denotes one internal parameter-update step performed by the nonlinear least-squares solver, rather than one complete

execution of the retrieval procedure or one forward-model evaluation. Solver iteration 0 represents the initial parameter deviation.

The original Fig. 5 showed the convergence of the retrieval errors averaged over the simulations at each altitude. However, this averaging obscured the convergence behavior of individual retrievals. To illustrate the process more clearly, Fig. R6 presents one example from the 100 simulation trials, showing the convergence of the retrieved temperature and wind velocity at different altitudes for both large (temperature: +20 K; wind velocity: +20 m s^{-1}; RB amplitude: +50%; Mie amplitude: −50%) and small (temperature: +5 K; wind velocity: +5 m s^{-1}; RB amplitude: +20 %; Mie amplitude: −20%) initial-guess deviations.

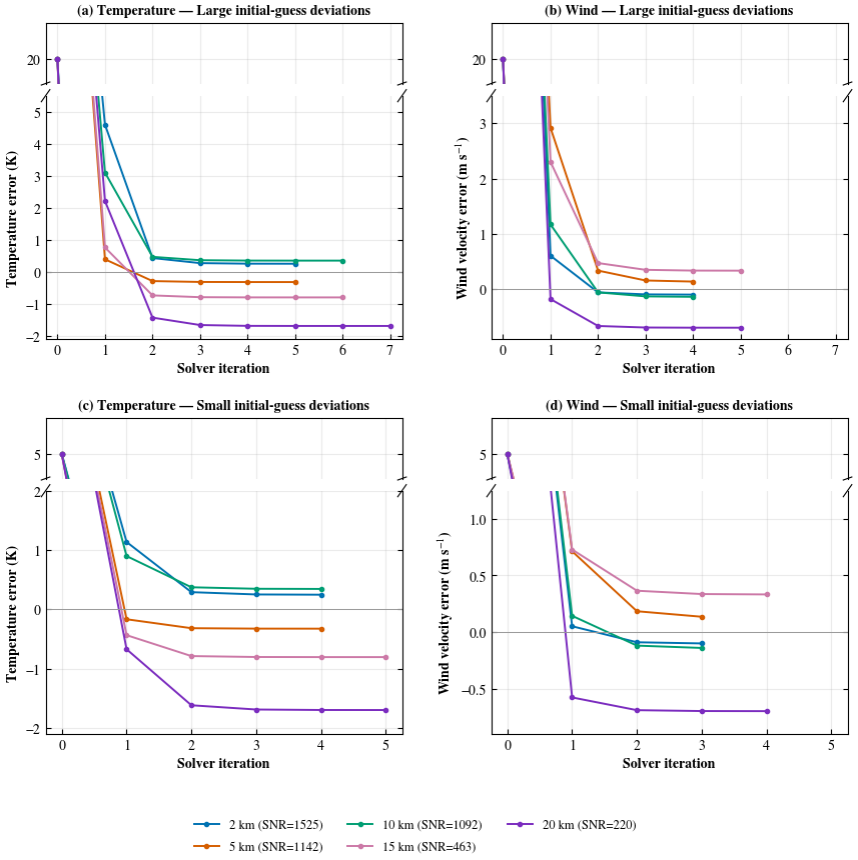


Figure R6. Convergence of temperature and wind velocity retrieval errors at five heights for the first Monte Carlo realization. Iteration 0 denotes initialization.

As shown in Fig. R6, the retrieval errors decrease substantially during the first iteration. However, this initial reduction does not indicate convergence; further iterations are required to refine the parameter estimates and satisfy the convergence criteria.

The revised Fig. 5 in the manuscript summarizes the mean number of iterations required for convergence over the 100 simulation trials, together with the corresponding temperature and wind velocity retrieval results at each altitude, for both large and small initial-guess deviations. For temperature retrieval, the number of iterations increases markedly as the SNR decreases, whereas for wind velocity retrieval, it varies only slightly over the simulated altitude range. Larger initial-guess deviations substantially increase the number of iterations required for convergence. Nevertheless, both initial-guess conditions yield closely consistent final retrievals, indicating that, within the tested conditions, the initial guess affects the convergence speed but has little effect on the converged results. The revised Fig. 5 is shown here as Fig. R7.

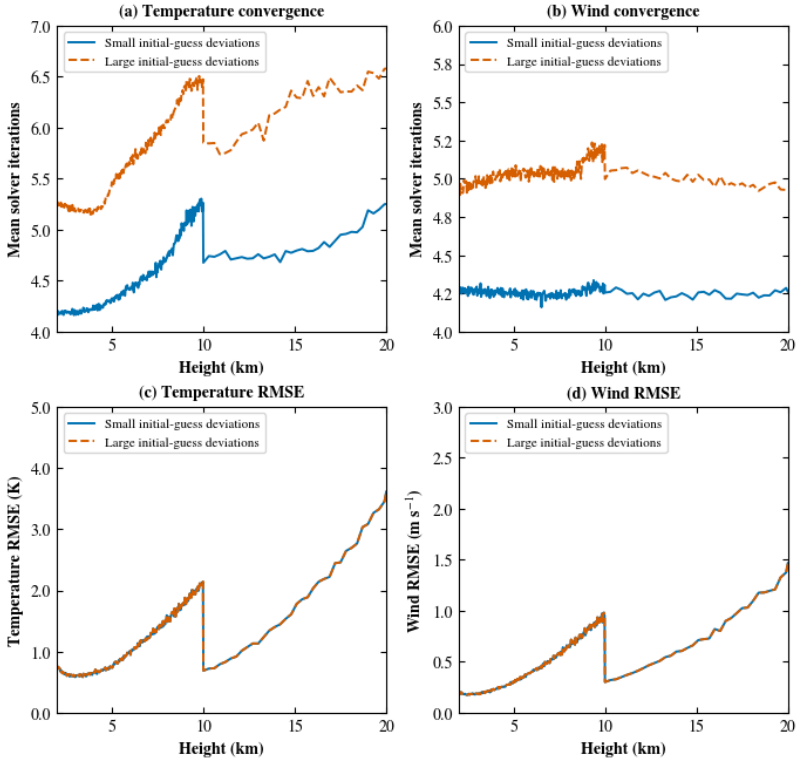


Figure R7. Comparison of mean solver iteration counts for (a) temperature and (b) wind velocity retrievals, and RMSEs of (c) temperature and (d) wind velocity.

The corresponding revisions can be found on page 12–13, lines 279–293 of the revised manuscript.

Comment 14)

It could be helpful to show a few exemplary RB spectra showing how they are used in this simulation, to get a better feeling for what you are analyzing. I would suggest showing both the spectra as well as the best fit, and the corresponding T, p, and Mie that were used for the simulation and retrieved from the fit. With that, the results shown in Fig. 6 could also be much better interpreted.

Response:

Thank you for this helpful suggestion. We have updated Fig. 6 by adding representative simulated photon-count distributions and their best-fit curves at 2 and 15 km. We have also added detailed simulation parameters and examples of the simulated spectra at each altitude to Appendix A.

During this re-examination of the simulations and retrieval implementation, we identified an inappropriate bound on the Mie intensity parameter that restricted its adjustment during fitting. Because temperature and Mie intensity are coupled in the retrieval, this constraint caused the temperature estimate to compensate, leading to an underestimation of temperature. The previously reported bias therefore arose from the parameter constraint in the retrieval implementation, rather than from the prescribed aerosol profile itself. The revised Fig. 6 is shown here as Fig. R8.

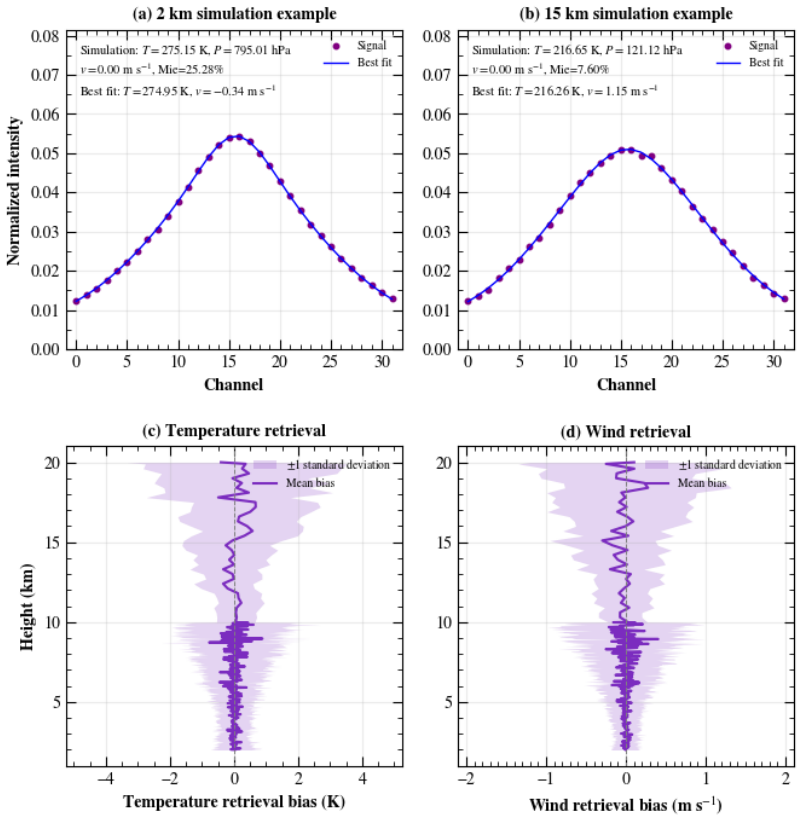


Figure R8. Examples of normalized simulated photon counts and their best fits at (a) 2 km and (b) 15 km. Mean retrieval biases and standard deviations of (c) temperature and (d) wind velocity as functions of height.

The revised results are presented on Pages 13–14, Lines 294–306, and the detailed simulation parameters and example spectra are provided in Appendix A on Page 24.

Comment 15)

For the transmission curve measurement that you show here, it is not clear if you use the same fiber (200 µm, NA = 0.22) that you also use for atmospheric measurements. Furthermore, the fiber illustrates that your imaging setup is defined such that you do not measure down to the "valley" of the transmission curve. This is even less true when the spectrum is convolved with the RB spectrum. This is something I do not understand. Although the edges of the spectrum do not contain many photons, the determination of the valley is important to determine the FWHM of the measured spectrum and hence the temperature. Why do you choose such an imaging configuration? Have you

performed simulations that would justify this approach?

Further, one point that is not discussed in the paper but that is very important is how you transfer the pixel position to a real frequency. Do you have a scannable laser for doing so? How stable is this over time?

Last but not least, the accuracy of the suggested technique significantly depends on a proper correction of the illumination function. How do you perform this correction? How stable is the illumination function over time?

Response:

Thank you for this comment and pointing this out. The transmission-curve calibration was performed using the same multimode fiber employed for the atmospheric measurements (200 μm core diameter and NA = 0.22). Moreover, the position and alignment of the fiber, as well as the entire receiver optical configuration, were kept unchanged between the calibration and atmospheric measurements. We have clarified this point in the revised manuscript.

We agree that sampling the transmission valley can provide useful information for determining the spectral width. However, the temperature in our method is not retrieved by directly measuring the FWHM between the peak and valley. Instead, it is obtained by fitting the complete photon-count distribution recorded by the 32 detector channels using the forward spectral model. The frequency interval represented by each detector channel increases with the Fizeau wedge angle. Therefore, a smaller wedge angle provides finer spectral sampling of the temperature-dependent line shape, although it reduces the total spectral range covered by the detector. To illustrate this trade-off, additional simulations were performed at 15 km using wedge angles of 3, 5, and 10 μrad under otherwise identical conditions. In addition, because a tunable etalon is employed in our receiver, the cavity length along the z-axis can be adjusted to shift the interference pattern, allowing the transmission valley to be experimentally accessed and characterized when required.

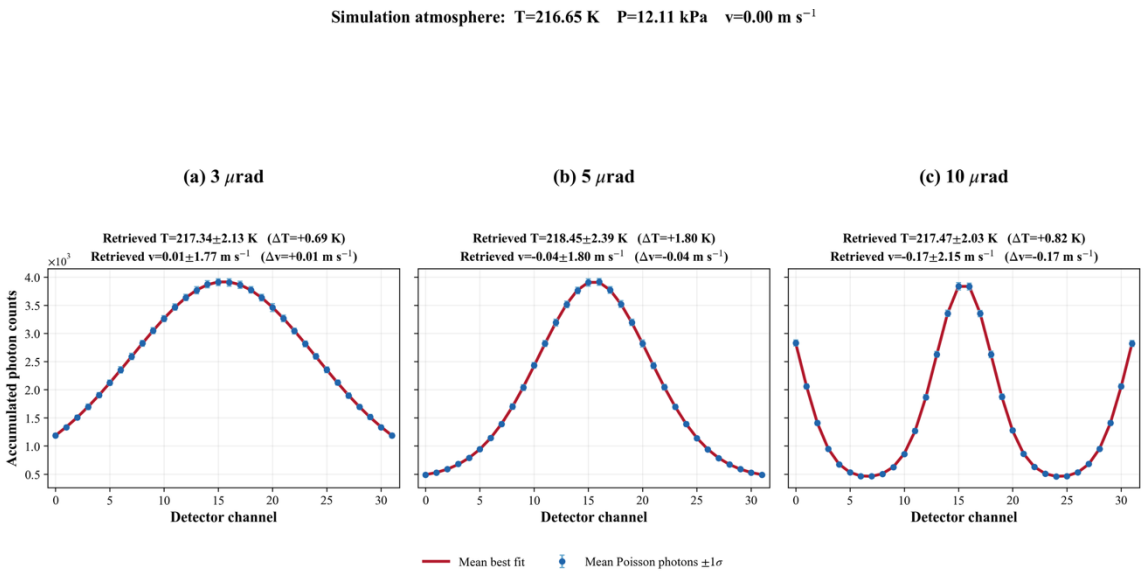


Figure R9. Simulated photon-count distributions and best-fit curves at 15 km for Fizeau wedge angles of (a) 3 μrad, (b) 5 μrad, and (c) 10 μrad.

The input temperature was 216.65 K. Based on 100 independent retrievals with a 5 min accumulation time, the mean retrieved temperatures were 217.34 ± 2.13, 218.45 ± 2.39, and 217.47 ± 2.03 K for wedge angles of 3, 5, and 10 μrad, respectively. The corresponding temperature biases were +0.69, +1.80, and +0.82 K. For an input radial wind speed of 0 m s^{-1}, the retrieved wind speeds were 0.01 ± 1.77, −0.04 ± 1.80, and −0.17 ± 2.15 m s^{-1}, respectively. These results demonstrate that, when retrieval is performed by fitting the complete spectral line shape, the absence of a distinct spectral valley does not adversely affect the retrieval. The fitting algorithm uses the intensity distribution across all detector channels rather than relying on the position or depth of a particular valley. A smaller wedge angle also maps a narrower frequency interval onto each pixel, providing finer spectral sampling. In addition, more returned photons are collected per channel on average, thereby improving the per-channel signal-to-noise ratio. Consequently, the 3 μrad configuration achieved the smallest temperature bias and the lowest wind-speed uncertainty among the three configurations. Under the present simulation conditions, a visible spectral valley is therefore not required for accurate retrieval, and the smaller wedge angle can provide comparable temperature precision and improved wind-speed precision.

The frequency-to-channel response of the receiver was experimentally calibrated using

a tunable continuous-wave laser. During the frequency-scanning experiment, the laser frequency was monitored using a wavelength meter, while the corresponding transmission-peak position on the 32-channel PMT array was determined. The frequency-to-channel conversion factor of 191 MHz channel^{-1} reported in the original manuscript represents the theoretical value calculated from the fitted wedge angle of the Fizeau interferometer and its free spectral range (FSR), rather than the experimentally measured response.

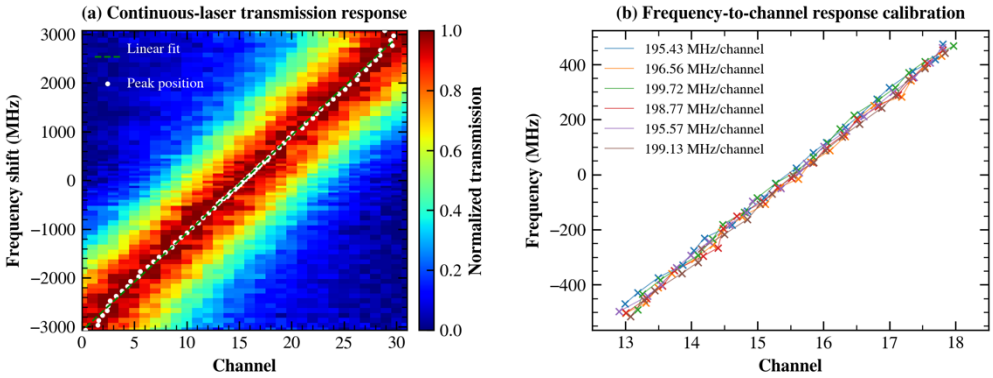


Figure R10. Calibration of the frequency-to-channel response. (a) Measured continuous-wave laser transmission response as a function of detector channel and laser frequency shift. The white dots indicate the fitted peak positions, and the dashed line represents the corresponding linear fit. (b) Frequency-to-channel response obtained from six independent frequency-scanning measurements, with the fitted slopes indicated in the legend (Revised Fig. 9 in manuscript).

To further clarify the experimental calibration, the measured frequency-to-channel response has now been added as Fig. 9 in the revised manuscript. As shown in Fig. R10(a), one frequency scan covered the full response range of the 32-channel detector. A nearly linear relationship between the laser frequency shift and the fitted peak position was observed over most of the detector range. Some deviations from linearity occur near the detector edges (around channels 0 and 31), mainly due to variations in the output energy of the tunable laser during the scan and the limited spectral information available for accurately determining the peak position when the transmission peak approaches the detector boundary.

For the atmospheric wind retrieval, the transmission peak primarily shifts within the central six channels, corresponding approximately to a Doppler-frequency-shift range

of −500 to 500 MHz. Therefore, the frequency-to-channel response was further characterized specifically within this effective working range. Six independent frequency-scanning measurements were performed, as shown in Fig. R10(b), yielding a mean response of 197.53 MHz channel^{-1} with a standard deviation of 1.90 MHz channel^{-1}. This experimentally determined response was used for the subsequent Doppler-frequency-shift determination and wind retrieval. The corresponding description has been added to the revised manuscript on Pages 16–17, Lines 334–358.

The illumination function was calibrated using a broadband LED light source, with the same 200 μm-core, NA = 0.22 multimode fiber that was used for the atmospheric measurements. The corresponding description has also been added to Pages 14–15, Lines 309–318 of the revised manuscript. The revised Fig. 7 is shown here as Fig. R11.

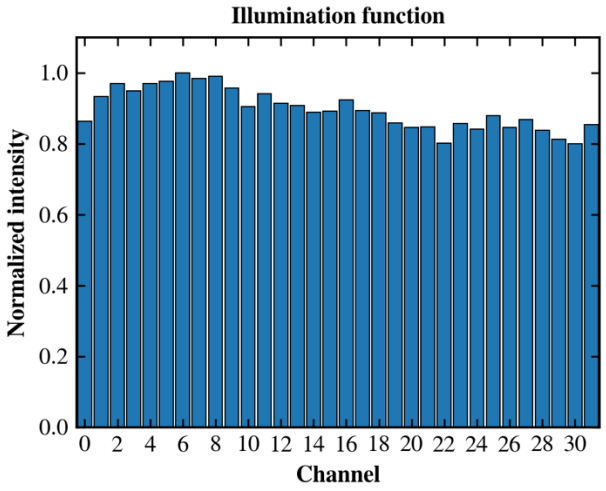


Figure R11. Illumination function of the 32-channel PMT array.

Before each atmospheric observation, the Fizeau transmission response was measured using the same pulsed laser employed for the atmospheric measurements. The repeatability of these measurements provides an indirect indication of the stability of the overall receiver response, including the illumination function.

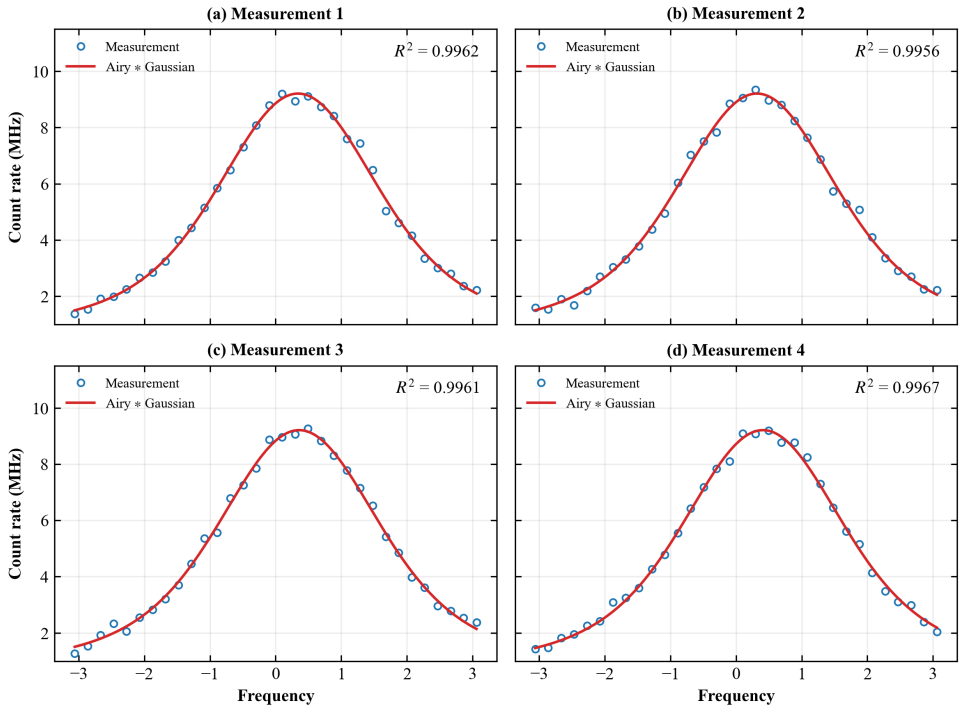


Figure R12. Receiver calibration results.

As shown in Fig. R12, the measured receiver responses exhibit good repeatability, indicating that the overall receiver response remained relatively stable under the tested conditions. This also provides indirect evidence that the illumination function was relatively stable.

Comment 16)

This figure actually illustrates the point I mentioned above. The measured raw signal does not reach the valleys. Furthermore, the shown spectrum is pretty asymmetric. I do not understand how you can retrieve such precise temperature and wind values from this raw signal. Could you clarify that? Could you show the best fit to these particular spectra and the fit values that you retrieve? Is the blue curve the best fit to the purple data points? If so, I think there must be something wrong. With such poor agreement, it should be impossible to derive correct parameters. But maybe I do not understand this correctly here.

Response:

Thank you for raising this important and constructive point. The issue that the measured

spectrum does not extend to the transmission valleys has been addressed in our response to Comment 15.

Regarding the apparent asymmetry, first, the spectral center does not coincide with the central channel of the PMT array, and therefore the measured spectral distribution is not expected to be symmetric with respect to the center of the detector. Second, the purple data points in the original figure represent the completely raw measured signal, without correction for the illumination function. Therefore, the nonuniform illumination distribution can contribute to the apparent asymmetry of the raw spectrum. Before retrieving the atmospheric parameters, the raw signal is corrected using the illumination function, as described in our response to Comment 15. We have revised the figure to show the illumination-corrected signal and updated the corresponding caption to make this processing step explicit and avoid ambiguity.

We also apologize that the meaning of the blue curve was not sufficiently clear. In the original figure, it represented the atmospheric scattering spectrum obtained after deconvolving the measured receiver response, rather than the best-fit curve to the purple data points. In the revised figure, we have replaced this deconvolved spectrum with the best-fit curve to the measured signal and included the retrieved parameter values, allowing the agreement between the measurement and the fit to be assessed directly. The revised Fig. 10 is shown here as Fig. R13.

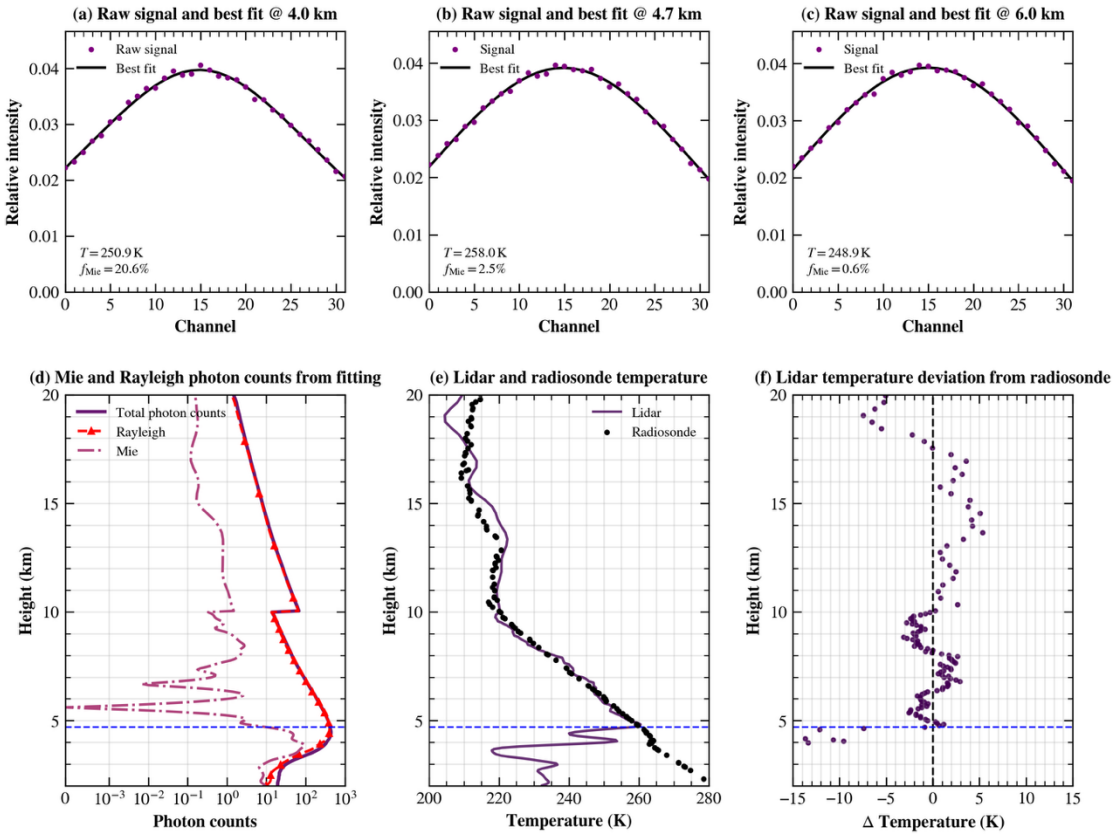


Figure R13. Spectral fitting results and evaluation of the influence of Mie scattering on temperature retrieval. (a–c) Best-fitting results of the measured signals at 4.0, 4.7, and 6.0 km. (d) Retrieved total, RB, and Mie photon counts. (e) Comparison between the lidar-retrieved and radiosonde temperature profiles. (f) Temperature difference (lidar minus radiosonde). The blue dashed line indicates the lower boundary of the temperature retrieval (4.7 km).

The revised figure is presented as Fig. 10 on Page 17.

Comment 17)

I do understand that the temperature retrieval is significantly impacted by Mie scattering, but the wind retrieval shouldn't be. As it is "just" a determination of the fringe position, this should also work in the vicinity of Mie scattering. Actually, it should even provide better results due to the higher signal levels. Could you clarify that? The wind profiles start already at 2 km but do not go down to the ground. Is this related to overlap issues?

Can you show further spectra for cloud returns and from the free atmosphere for comparison? Also, could you show the best-fit result? It is also not clear how you

retrieve the wind. What is your reference?

Response:

Thank you for this insightful comment. We agree with the reviewer that, unlike temperature retrieval, which is sensitive to the spectral shape and can therefore be significantly affected by enhanced Mie scattering, wind retrieval mainly relies on the determination of the spectral center. Therefore, enhanced Mie scattering does not fundamentally prevent wind retrieval and may even improve the statistical precision due to the increased signal level. We have revised the manuscript accordingly to clarify this point on Page 21, Lines 413-424. In addition, we have further clarified that the radiosonde launch site was located approximately 100 km from the lidar observation site, this information has been added to the revised manuscript on Page 19, Line 393. The relatively large wind-speed deviations observed at lower altitudes may therefore partly arise from spatial inhomogeneity in the tropospheric wind field, as the lidar and radiosonde sampled the atmosphere at different locations.

Regarding the lower limit of the wind profiles, the lidar system employs a bistatic transmitter–receiver configuration. In the near-field region, the transmitted laser beam and the receiver field of view do not geometrically overlap, preventing reliable wind retrieval down to the ground. This limitation has been clarified in the revised manuscript on Page 18, Lines 387–388.

To provide a more direct comparison, we have added representative measured spectra from a cloud-affected region and from the free atmosphere. Fig. R14 shows the measured spectra and the corresponding best-fit results at approximately 5 km and 10 km.

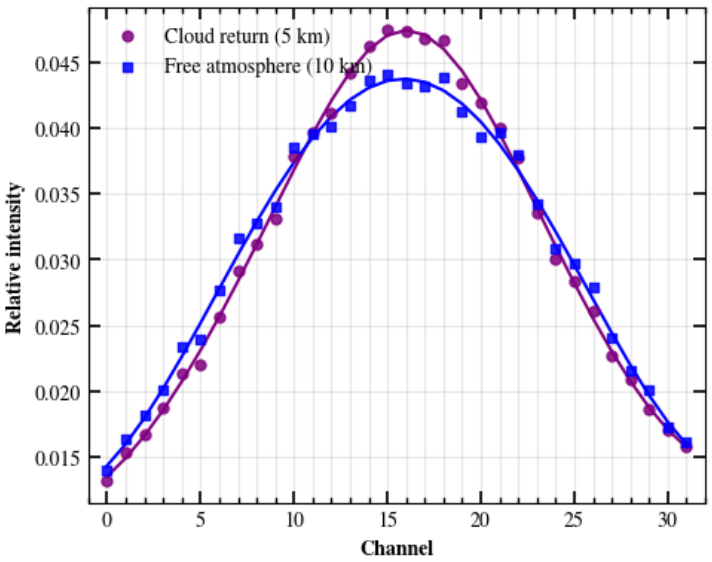


Figure R14. Measured spectra and corresponding best-fit results for a cloud-affected return at 5 km and a free-atmospheric return at 10 km.

The laser frequency was continuously monitored by a wavelength meter during the atmospheric measurements, providing a real-time reference for the transmitted laser frequency. Since our system operates as a scanning Doppler wind lidar, measurements were performed in opposite viewing directions. The wind component was then derived from the difference between the Doppler velocities measured in the two opposite directions. In this way, common systematic frequency offsets are largely cancelled, while the atmospheric Doppler contribution changes sign and is retained. We have clarified the wind retrieval procedure and its frequency reference in the revised manuscript on Page 20, Lines 403–408. The Doppler velocities retrieved for the individual viewing directions before the opposite-direction subtraction are shown in Fig. R15.

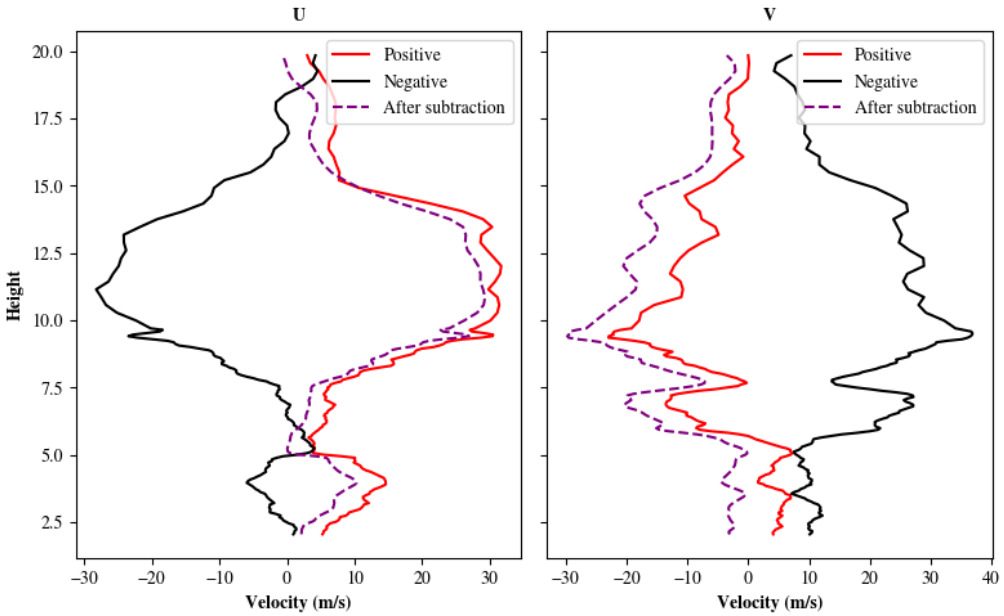


Figure R15. Opposing-direction measurements of the lidar-derived U and V wind components.

References in this response:

Hagen, N., Kupinski, M., and Dereniak, E. L.: Gaussian profile estimation in one dimension, Applied Optics, 46, 5374-5383, 10.1364/AO.46.005374, 2007.

McKay, J. A.: Assessment of a multibeam Fizeau wedge interferometer for Doppler wind lidar, Applied Optics, 41, 1760-1767, 10.1364/AO.41.001760, 2002.

Vaughan, M., Ridley, K., Witschas, B., Lux, O., Nikolaus, I., and Reitebuch, O.: Spectral performance analysis of the Fizeau interferometer on board ESA's Aeolus wind lidar satellite, ATMOSPHERIC MEASUREMENT TECHNIQUES, 18, 2149-2181, 10.5194/amt-18-2149-2025, 2025.

Witschas, B.: Analytical model for Rayleigh–Brillouin line shapes in air, Applied Optics, 50, 267-270, 10.1364/AO.50.000267, 2011a.

Witschas, B.: Analytical model for Rayleigh–Brillouin line shapes in air: errata, Applied Optics, 50, 5758-5758, 10.1364/AO.50.005758, 2011b.

Witschas, B., Vieitez, M. O., van Duijn, E.-J., Reitebuch, O., van de Water, W., and Ubachs, W.: Spontaneous Rayleigh–Brillouin scattering of ultraviolet light in nitrogen, dry air, and moist air, Applied Optics, 49, 4217-4227, 10.1364/AO.49.004217, 2010.

Response to Referee#2

We thank the referee for the careful assessment of our manuscript and for the constructive comments on the receiver characterization, calibration procedures, retrieval performance, and uncertainty assessment.

Comment 1)

Lines 13–16: The authors statement "To overcome this limitation" is not completely valid because the described approach only partially addresses the signal contamination problem by Mie scattering. In this manuscript the temperature retrievals are limited to 5.3 km and above. Please rephrase the statement to indicate that the technique partially addresses the contamination problem.

Response:

We agree that the original wording was not sufficiently precise. Resolving the atmospheric spectrum provides information for distinguishing molecular and particle scattering, but it does not eliminate the influence of Mie scattering on temperature retrieval. These revisions have been made in the Abstract on Page 1, Lines 13–18 and 24–26, and Page 2, Lines 54–62.

Comment 2)

Line 45: An alternative approach for atmospheric temperature profiling that is immune to contamination by Mie scattering is based on iodine-vapor-filter HSRL. Please consider referring to this alternative approach and cite the relevant work by Hair et al., "High-Spectral-Resolution Lidar with Iodine-Vapor Filters: Measurement of Atmospheric-State and Aerosol Profiles," Applied Optics, 40, 5280–5294 (2001).

Response:

Thank you for suggesting this relevant reference. We have added Hair et al. (2001) to the Introduction and acknowledge iodine-vapor-filter HSRL as an alternative approach for atmospheric-state profiling and molecular–particle discrimination. The corresponding text has been added on Page 3, Lines 72–73.

Comment 3)

Line 176 and Fig. 2(a): The authors state that the instrument has a coaxial transmitter–receiver configuration. However, the conceptual image shows a biaxial arrangement of the instrument. The biaxial configuration would explain the lower 2km blind zone that is not discussed in the manuscript. Please clarify the instrument configuration.

Response:

Thank you for pointing out this inconsistency. The original description of the transmitter–receiver configuration was incorrect and has been corrected in the revised manuscript (Page 8, Line 181).

Comment 4)

Line 178: It is likely that the instrument's hardware components such as wavelength meter as well as the laser frequency locking scheme and frequency long term stability were previously described in earlier papers. However, it would be valuable to either provide more detailed hardware description in this manuscript or to refer to the previously published paper that includes more details.

Response:

Thank you for this suggestion. We have expanded the hardware description to specify the wavelength meter and seed laser models and clarify the frequency-stabilization scheme. A small fraction of the transmitted 355 nm beam is monitored by a wavelength meter (HighFinesse, WS8-2), and the measured wavelength is fed to a custom-built PID controller for feedback control of the 1064 nm seed laser (NKT Photonics, K8230). These details have been added on Page 8, Lines 181–184.

Comment 5)

Line 185: Please consider specifying the manufacturer and model number of the linear PMT array.

Response:

Thank you for this suggestion. We have added the manufacturer and model of the linear

PMT array (Hamamatsu, H11460-200) to the revised manuscript (Page 11, Line 266).

Comment 6)

Equation (12): Equation 12 estimates the number of the photons detected by each channel. Assuming the convolution with the transmission function of the receiver accounts for the fraction of the N total photons in each channel, dividing N(z) received photons by N number of channels can be a duplicate in normalization. Please clarify the normalization in the Equation 12.

Response:

Thank you for pointing out this ambiguity. We have revised Eq. (13) to explicitly integrate the convolved spectral response over the effective width of each detector channel. Under the stated ideal assumptions, $N(z)/\mathrm{L_{if}}$ represents the spatially uniform incident count density, while the convolved response accounts for the frequency-dependent transmission of the Fizeau interferometer. We have also clarified that the combined molecular and Mie spectrum is normalized to unit area. This formulation replaces the original division by the number of channels and clarifies the normalization (Lines 233–242). The revised Eq. (13) is shown below.

$$N_j(y_j, \nu, z, T) = \frac{N(z)}{\mathrm{L_{if}}} \cdot \int_{y_j-\Delta y/2}^{y_j+\Delta y/2} \{[S_{rb}(\nu, z, T) + S_{Mie}(\nu)] \otimes F(\nu - \nu(y)) \otimes S_{laser}(\nu)\}\, dy$$

Comment 7)

Line 230: Please revise the terminology regarding returns and detector counts: “the total number of returned photons”. The dark counts do not contribute to the “returned photons” since they do not originate from the returned photons, but rather contribute to the total number of counts. Please distinguish consistently between “returned photons” and total number of counts.

Response:

Thank you for pointing out this terminology issue. We have replaced “the total number of returned photons” with “the total expected counts” to distinguish the atmospheric return from detector dark counts and background counts (Line 239).

Comment 8)

Lines 240–250: The optimization problem is a trade-off due practical constraints and often does not have a single optimal solution. According to the presented metric shown in Figure 3, the optimum detector channel number appears to be 16. However, the performance is not significantly different between cases for 8 and 128 channels provided the proposed metric has an offset of only 1km. Intuitively, with increasing number of detectors the dark counts start to dominate the returns and degrade SNR. The opposite is true for decreasing number of detectors. What is the minimum number of spectral bands are required for the accurate measurements? The presented color map shown in the Figure 3 has a vertical resolution of 1 km. Later in the manuscript the profile retrievals use coarse 300 m vertical resolution above 10km. It is unclear whether the calculations demonstrated in Figure 3 are accounting for larger vertical integration above 10 km or authors use 1km vertical resolution in the modeling. Please clarify.

Response:

Thank you for this valuable comment. Your insightful suggestions prompted us to reconsider our approach to optimizing the number of detector channels and to conduct a more comprehensive and realistic numerical simulation. In the revised simulation, we adopted the same vertical resolution as that used in the atmospheric measurements, with 60 m below 10 km and 300 m above 10 km. Furthermore, we directly evaluated the performance of different channel configurations at each altitude using the root mean square errors (RMSEs) of the retrieved temperature and wind velocity. Seven detector configurations with 4, 8, 16, 32, 64, 128, and 256 channels were investigated in the revised simulations.

Hagen et al. examined the effects of sampling density, finite pixel width, and noise on the estimation of Gaussian spectral parameters, highlighting the importance of balancing spectral sampling resolution and measurement uncertainty (Hagen et al., 2007). Our retrieval method is based on spectral fitting and involves four free parameters. Therefore, at least four spectrally independent measurements are required for parameter estimation, making four channels the theoretical minimum for our

retrieval approach. Furthermore, our simulation results demonstrate that the four-channel configuration can also achieve relatively good retrieval accuracy. Increasing the number of channels provides only limited improvement in retrieval accuracy, while configurations with larger numbers of channels may even exhibit degraded performance due to reduced signal-to-noise ratios (SNRs), as illustrated in the revised Fig. 3. Ultimately, the 32-channel configuration was selected as a compromise among overall system robustness, complexity, and the commercial availability of multichannel PMT arrays. The revised Fig. 3 is shown here as Fig. R1.

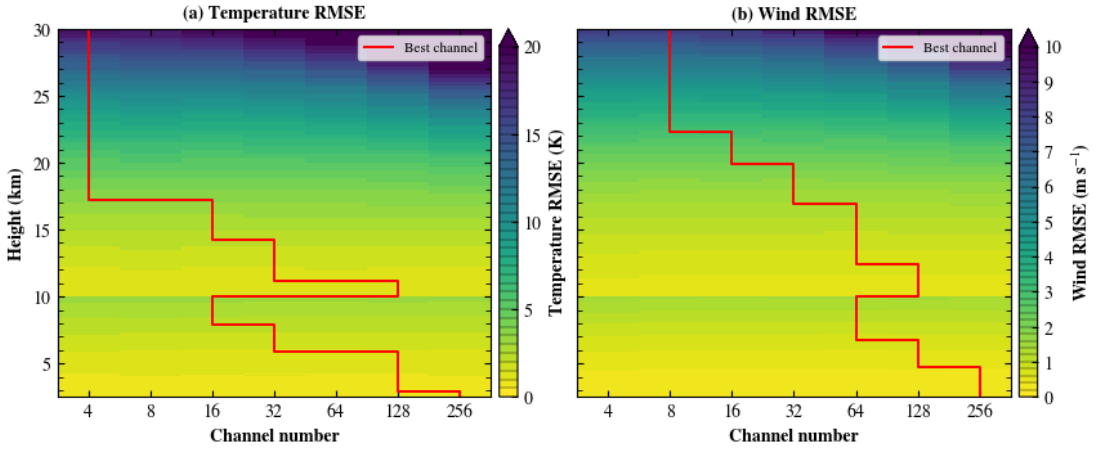


Figure R1. Influence of detector channel number and detection height on the retrieval accuracy of (a) temperature and (b) wind velocity.

The corresponding revisions can be found on Pages 10–11, Lines 244–267.

Comment 9)

Section 4, Fig. 5: The authors show a rapid convergence of their retrieval algorithms demonstrating a mean error across the altitudes 2-4 km and 5-20 km. Please explain how the algorithm is converging within single cycle independent of the amplitude of the original perturbation and whether it demonstrates the same convergence rate when multiple parameters are perturbed. Convergence of the mean error of the retrieval do not represent the convergence of retrievals at individual altitudes. Assuming Figure 6 represents the converged result of the same simulation, it then demonstrates the

resulting biases of the retrievals at individual altitude rather than the mean error of the profile. It would be more indicative of the successful convergence if the authors can demonstrate the convergence for individual retrievals.

Response:

Thank you for this valuable comment. Your observations are well-founded and have prompted us to conduct a more comprehensive analysis of the convergence behavior of our retrieval algorithm. In response to your suggestions, we performed a new set of numerical simulations using a vertical resolution of 60 m below 10 km and 300 m above 10 km. Furthermore, we systematically investigated the convergence behavior of the temperature and wind velocity retrievals at individual altitudes, the effects of simultaneous deviations in the initial guesses of multiple parameters, and the resulting retrieval accuracy.

First, we would like to clarify that our retrieval algorithm does not converge within a single iteration. When the initial guesses deviate substantially from the true parameter values, the first iteration may produce a relatively large reduction in retrieval errors; however, several additional iterations are still required to achieve convergence. Furthermore, larger deviations in the initial guesses generally require more iterations for both temperature and wind velocity retrievals to converge compared with smaller initial deviations. To demonstrate this behavior, we selected a representative case from our numerical simulations, as shown in Fig. R2.

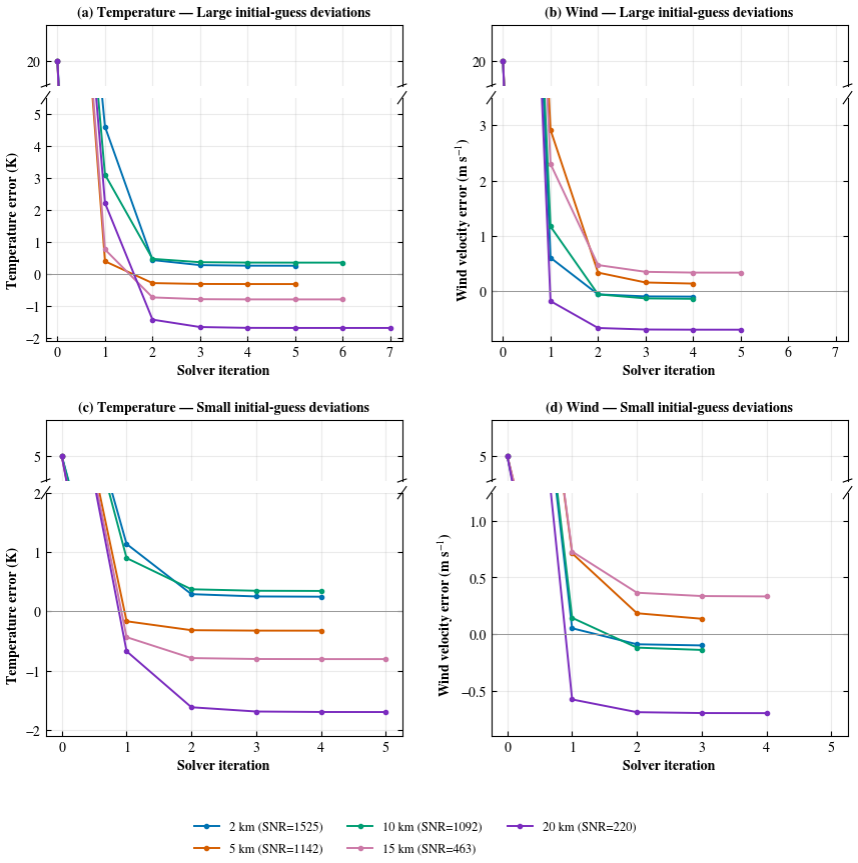


Figure R2. Convergence of temperature and wind velocity retrieval errors at five heights for the first Monte Carlo realization. Iteration 0 denotes initialization.

Figure R2 illustrates the convergence of the first of the 100 Monte Carlo realizations as an example. The plotted cases included small initial-guess deviations (temperature: +5 K; wind velocity: +5 m s^{-1}; RB amplitude: +20 %; Mie amplitude: −20%) and large initial-guess deviations (temperature: +20 K; wind velocity: +20 m s^{-1}; RB amplitude: +50%; Mie amplitude: −50%), applied simultaneously to the initial values of all four parameters. The temperature and wind velocity retrievals stabilize within a few solver iterations at all five heights. Larger initial-guess deviations generally require more iterations.

The revised Fig. 5 presents the altitude-dependent mean number of iterations required for temperature and wind velocity retrievals to converge under different initial-guess deviations, based on 100 simulation runs. It also shows the RMSEs of the retrieved temperature and wind velocity for different initial-guess deviations. The results demonstrate that the retrieval algorithm achieves convergence at all investigated

altitudes, with nearly identical converged values across different initial guesses. Although larger initial-guess deviations generally increase the number of iterations required for convergence, they have a negligible influence on the final retrieval accuracy. The revised Fig. 5 is shown here as Fig. R3.

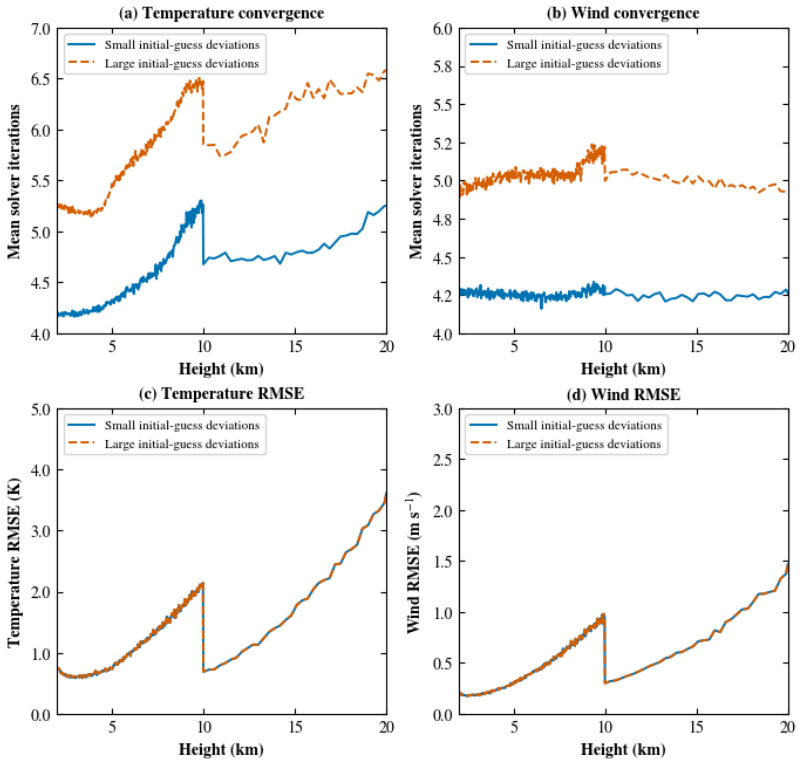


Figure R3. Comparison of mean solver iteration counts for (a) temperature and (b) wind velocity retrievals, and RMSEs of (c) temperature and (d) wind velocity.

The corresponding revisions can be found on pages 13–14, lines 305–331 of the revised manuscript.

Comment 10)

Fig 6, lines 285–289: The authors state “As shown in Fig. 6, the retrieved temperature exhibits a noticeable negative bias between 2 and 4 km. This underestimation is mainly caused by the increasing contribution of Mie scattering in the lower troposphere.” However, authors do not explain an introduced contamination by Mie signal for the presented modeling result. In my opinion, the temperature retrieval bias profile shown in Figure 6(a) experience a positive linear trend below 5km. This is hard to attribute it

to an existence of such aerosol gradient in the lower atmosphere up to 5km. Please, provide an explanation on the mechanism that causes this bias or explain the modeling process if aerosol profile was used in the model to intentionally introduce the bias.

Response:

We thank the reviewer for questioning our previous interpretation. Upon re-examining the retrieval implementation, we identified an inappropriate bound on the Mie intensity parameter that restricted its adjustment during the fitting. Because temperature and Mie intensity are coupled, this restriction caused the temperature estimate to compensate, resulting in an underestimation. The previously reported bias therefore arose from the parameter constraint in the retrieval implementation, rather than from the prescribed aerosol profile itself.

We have corrected this constraint and repeated the simulations and retrievals. We also revised the simulation range resolution to match that used in the actual observations: 60 m below 10 km and 300 m above 10 km. The updated results, now presented in Fig. 6, no longer show the previously reported systematic temperature underestimation in the lower-height region. We have consequently removed the statement attributing that bias to an increasing Mie contribution. Appendix A has also been added to document the simulation settings, atmospheric profiles, and representative simulated signals.

The corresponding revisions can be found on pages 13–14, lines 294–306 of the revised manuscript. Appendix A is provided on page 24. The revised Fig. 6 is shown here as Fig. R4.

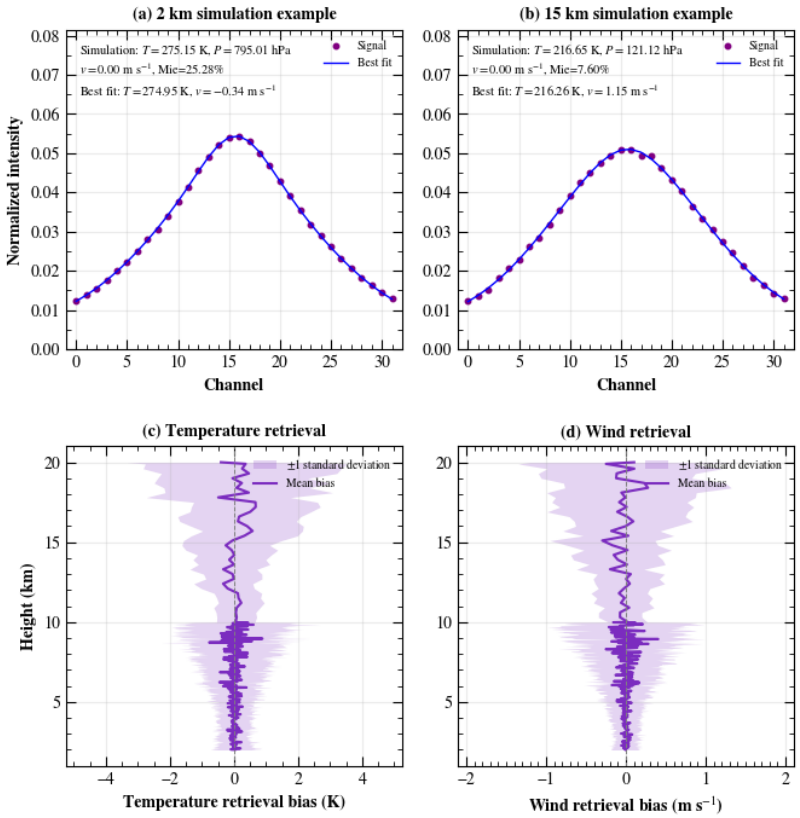


Figure R4. Examples of normalized simulated photon counts and their best fits at (a) 2 km and (b) 15 km. Mean retrieval biases and standard deviations of (c) temperature and (d) wind velocity as functions of height.

Comment 11)

Fig 8(a–c): The authors report the measured and the fitted spectra at 4.5, 4.6, and 4.7 km with changing contribution of Mie scattering. Based on the width of the Mie peak in the modeled spectra, the fitted curve represents a model of RB + Mie spectra not convoluted with the instrument function (laser spectra and receiver's transmission function). However, the authors comparing the calculated RB spectra with the measured one. Please explain the purpose of such comparison. In my opinion, the shape of the measured curves is asymmetric and visually would not be even closely matching the fitted curve once it is convoluted with the measured transmission functions and laser spectrum from Figure 7. The fitted curves have narrow peak from Mie scattering that does not appear in the measured signals even at 4.5 km. I believe, the asymmetry in the

measured spectra is indicative of the asymmetry in the receiver's transmission function. For reference, Figure 7 shows a measured receiver's transmission functions in the laboratory setting with a much smaller skewness. I assume that field measured spectra are affected by the difference in illumination of the Fizeau vs in the laboratory setting, or less likely by possible etalon/Fizeau drift. Please explain such large discrepancy in the two spectra and describe the correction procedure of the transmission function that allows to achieve such a good accuracy for the temperature profile above 5.3 km. Also, the lidar temperature profiles presented in the Figure 8 do not appear to have a native resolution of 60 m below 10 km and 300 m above 10 km. Please specify what type smoothing was applied to the profile and present an unsmoothed version of the lidar temperature profile.

Response:

Thank you for this valuable comment. We first acknowledge an error in the original calculation of the Mie scattering fraction. After correcting this calculation, the retrieved Mie fractions were higher than those reported in the previous version of the manuscript. We have updated the corresponding results and discussion accordingly.

We would also like to clarify the purpose of presenting the spectra in Fig. 8(a–c). Our retrieval algorithm can reconstruct the atmospheric backscattered spectrum, including both Rayleigh–Brillouin (RB) and Mie scattering components. These spectra were originally presented to illustrate how different Mie scattering contributions affect the spectral shape. In the revised figure, we have removed the atmospheric scattering spectra obtained by deconvolution and instead present the best-fit results alongside the measured signals, allowing a direct comparison in the measurement domain. To further illustrate the influence of Mie scattering on the spectral shape, we have replaced the examples with results at heights of 4, 4.7, and 6 km, representing different Mie scattering contributions. The revised Fig. 10 is shown here as Fig. R5.

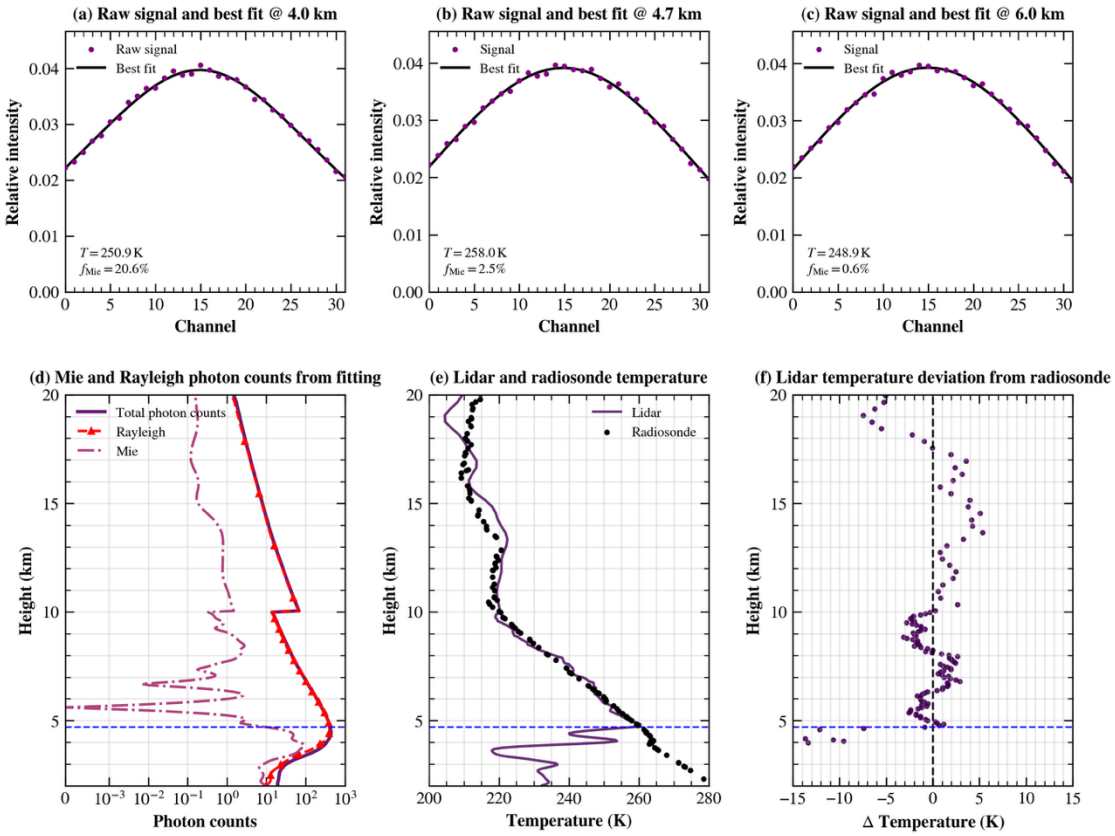


Figure R5. Spectral fitting results and evaluation of the influence of Mie scattering on temperature retrieval. (a–c) Best-fitting results of the measured signals at 4.0, 4.7, and 6.0 km. (d) Retrieved total, RB, and Mie photon counts. (e) Comparison between the lidar-retrieved and radiosonde temperature profiles. (f) Temperature difference (lidar minus radiosonde). The blue dashed line indicates the lower boundary of the temperature retrieval (4.7 km).

Regarding the reviewer's concern about why the narrow Mie scattering peak is not clearly observed in the measured spectra, we would like to clarify that the molecular (Rayleigh–Brillouin) and aerosol (Mie) scattering components are superimposed in the measured spectrum. Due to the finite spectral resolution of the Fizeau interferometer, the intrinsically narrow Mie scattering component is significantly broadened after convolution with the instrument response function. Consequently, the Mie scattering contribution affects the overall spectral shape rather than appearing as a distinct narrow peak.

To further demonstrate this effect, we performed additional simulations based on Eq. (13) of the manuscript. The ideal measurement spectra were calculated for four different Mie scattering fractions: 15%, 10%, 5%, and 0%. These simulations illustrate how the

narrow Mie scattering component is broadened by the instrument response and superimposed on the broader Rayleigh–Brillouin spectrum, thereby modifying the overall measured spectral shape without producing a clearly distinguishable narrow peak. The simulation results are presented in Fig. R6.

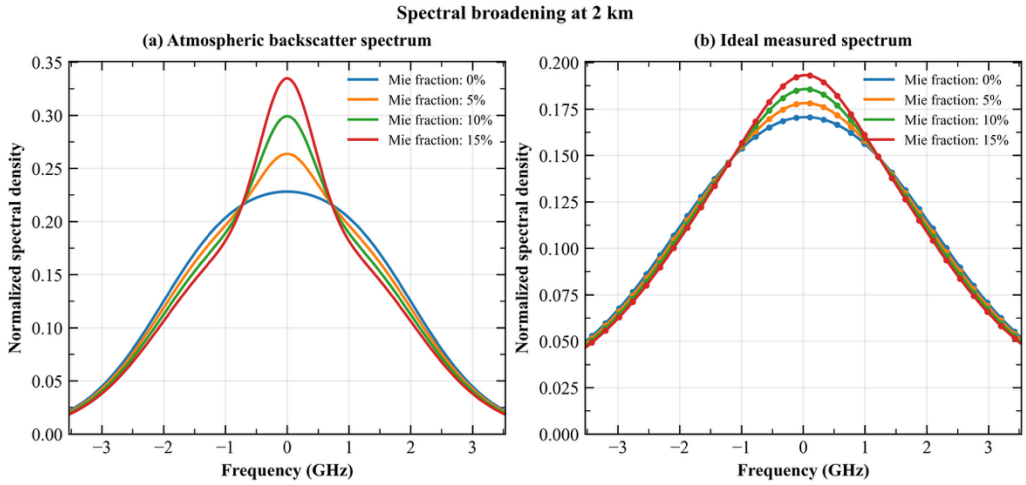


Figure R6. (a) Atmospheric backscatter spectra broadened by the laser linewidth and (b) ideal responses after transmission through the Fizeau interferometer at 2 km for Mie fractions of 0%, 5%, 10%, and 15%.

We apologize for the confusion caused by the presentation of the measured spectra. We would like to clarify that the spectra shown in the figure represent the raw photon counts recorded by the photon-counting acquisition system, without correction for the illumination function of the 32-channel PMT array. The nonuniform illumination across the detector channels can contribute to the apparent asymmetry of the measured spectra. To address this issue, we have added a detailed description of the illumination function calibration and correction procedure in the revised manuscript (Page 15, Lines 309–318). The added Fig. 7 is shown here as Fig. R7.

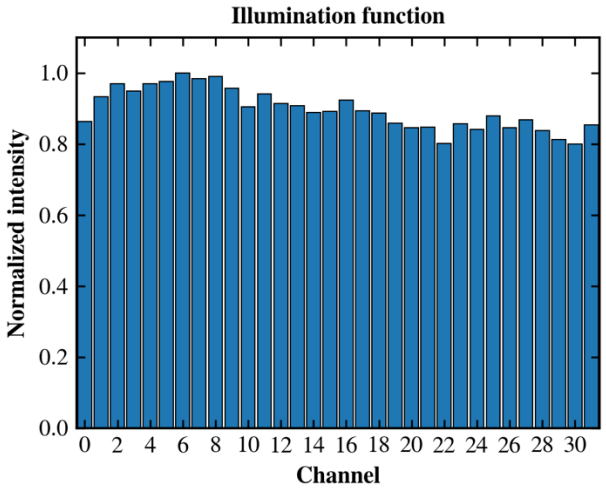


Figure R7. Illumination function of the 32-channel PMT array.

Furthermore, we have replaced the originally presented spectra with the illumination-function-corrected photon-counting signals and included the corresponding best-fit curves for comparison. The revised results are shown in Fig. R5

Regarding the reviewer's concern about the apparent inconsistency in the vertical resolution of the temperature profiles, we would like to clarify that the temperature profiles presented in the original manuscript were smoothed using a Gaussian filter with a standard deviation of $\sigma = 1.5$ data points to reduce small-scale fluctuations and better illustrate the overall vertical temperature structure.

In Fig. R8, we present the original unsmoothed temperature profile and the corresponding Gaussian-smoothed temperature profile based on the data shown in the Fig. R5(e).

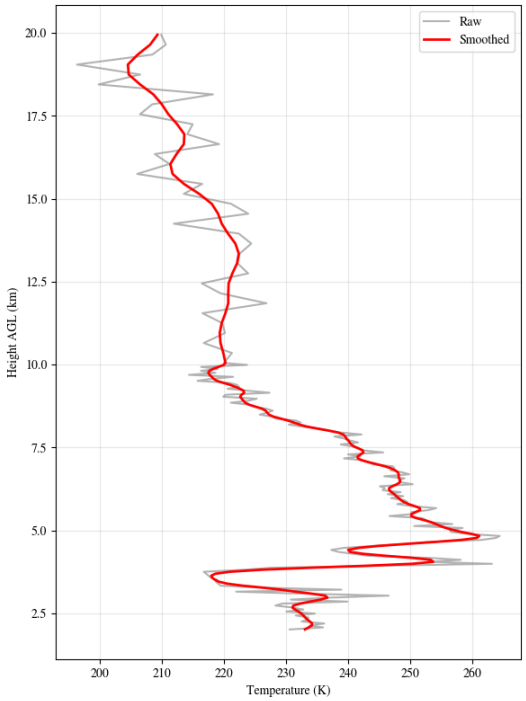


Figure R8. Comparison of the original unsmoothed temperature profile (Raw) and the Gaussian-smoothed temperature profile (Smoothed, σ = 1.5 data points) corresponding to Fig. R5(e).

Comment 12)

Table 1: Please include in the table 1 more technical parameters of the hardware: the laser manufacturer and model, frequency-locking accuracy, and long-term frequency drift as these are important parameters for reliable operation. Table 1 contains the duplicated "Transceiver" headings. Please replace them with "Transmitter" and "Receiver" where appropriate. Later in the manuscript authors report the laser linewidth of 0.67 GHz, while in the table the specified value is "<1GHz". Consider replacing it with more accurate value of 0.67GHz. Please also clarify what optical components "optical efficiency" parameter accounts for.

Response:

Thank you for this valuable comment. We have revised the manuscript to provide additional technical details regarding the laser system. Specifically, the manufacturer and model information of the laser system have been added on Page 7, Lines 174–180.

In addition, the frequency-locking accuracy has been included in Table 1 of the revised manuscript to provide a more comprehensive description of the laser's frequency stability performance. We have also replaced the duplicated “Transceiver” headings with “Transmitter” and “Receiver” and updated the laser linewidth to approximately 0.67 GHz.

Regarding long-term frequency drift, our laser system employs an active frequency-locking module to suppress frequency variations during operation. During the 46-minute monitoring period, no clear monotonic trend was observed in the measured laser frequency, and the standard deviation of the frequency fluctuations was 5.26 MHz as shown in Figure R9. These results indicate that frequency drift was limited over the monitored period.

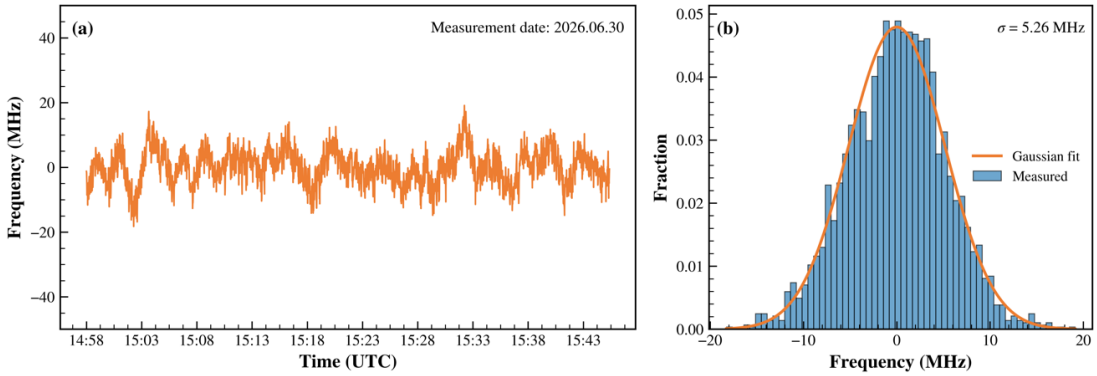


Figure R9. Laser frequency fluctuations measured by a wavelength meter during the atmospheric observation period.

Regarding the optical efficiency listed in Table 1, we would like to clarify that this parameter refers to the overall optical transmission efficiency of the optical components before the received light enters the receiver fiber.

Comment 13)

Table 2: In Table 2 authors specify parameters for the Fabry-Perot etalon. However, it is unclear if this parameters are for the original etalon, or when it is setup to operate in Fizeau interferometer mode. The plates misalignment will affect the peak transmission and the spectral bandwidth. I believe, the “spacer thickness” is more commonly used

terminology than “spacer length”.

Response:

Thank you for this valuable comment. To avoid ambiguity, we have revised Table 2 by replacing the original design parameters of the Fabry–Perot etalon with the corresponding parameters of the Fizeau interferometer used in our lidar system. The revised table now reflects the configuration of the Fizeau interferometer. In addition, we have replaced "spacer length" with "spacer thickness" as suggested by the reviewer. The revised Table 2 is shown here as Table R1.

Table R1. Parameters of the Fizeau interferometer.

Fizeau		
	Peak Transmittance (%)	67
	Spacer Thickness (mm)	12.5
	Mean Plate Reflectivity (%)	≈66
	Measured FWHM (GHz)	2.92
	Measured wedge angle (μrad)	2.83

Comment 14)

Please demonstrate the measured spectra and the fitted RB function convoluted with laser spectrum and receiver transmission spectra for the aerosol free altitude above 5.3 km with robust temperature measurement as a good example of the fit.

Response:

Thank you for this valuable suggestion. To further demonstrate the reliability of our spectral fitting method, we have provided an example of the measured and best-fit spectra at an altitude of 10 km, where the contribution of aerosol scattering is relatively weak.

The measured spectrum was corrected using the experimentally determined illumination function of the 32-channel PMT array. The best-fit spectrum was calculated using our forward model, which accounts for the Rayleigh–Brillouin

scattering spectrum, the laser spectral linewidth, and the spectral response of the Fizeau interferometer.

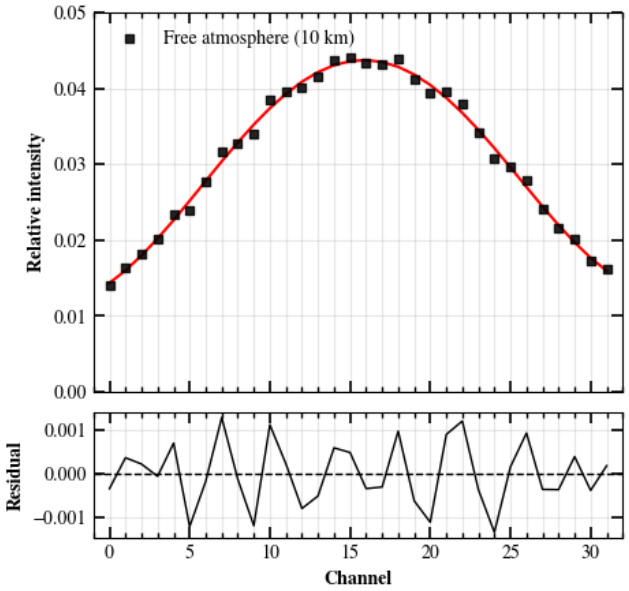


Figure R10. Comparison of the measured spectrum (black squares) and the best-fit spectrum (red solid line) at an altitude of 10 km under free-atmosphere conditions.

As shown in Fig. R10, the fitted spectrum agrees well with the measured spectrum across the detector channels, demonstrating the ability of the proposed retrieval method to reproduce the observed spectral characteristics for the aerosol free altitude.

Comment 15)

Please provide an example with a thin cirrus cloud to demonstrate that Mie scattering signal contamination is entirely confined within the cloud. That will demonstrate how robust the temperature measurements are. The attenuated backscatter profile would be useful for this assessment.

Response:

Thank you for this valuable suggestion. We conducted atmospheric observations under thin-cloud conditions, with a cloud layer located between approximately 8 and 9 km. To characterize the vertical distribution of the cloud layer, we calculated the normalized range-corrected signal profile from the measured photon-counting signals by applying background subtraction and range-squared correction. During the atmospheric

measurements, the telescope was tilted at an angle of 15°, which could introduce slight structural deformation and make it difficult to accurately correct for the geometrical overlap factor. Therefore, to minimize the influence of uncertainties associated with the overlap correction, we present the normalized range-corrected signal profile only above 6 km. The resulting profile is shown in Fig. R11.

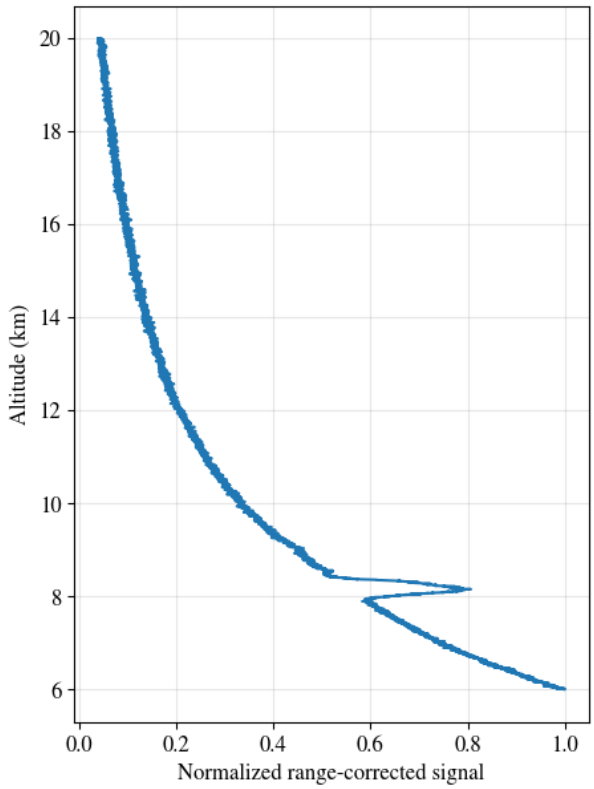


Figure R11. Normalized range-corrected lidar signal derived from the photon counts recorded by the 32-channel PMT array, after background subtraction and range-squared correction, assuming complete transmitter–receiver overlap above 6 km.

However, no radiosonde measurements were available for comparison on that observation day. Nevertheless, we have presented the temperature profile retrieved from the lidar measurements conducted on the same day in Fig. R12.

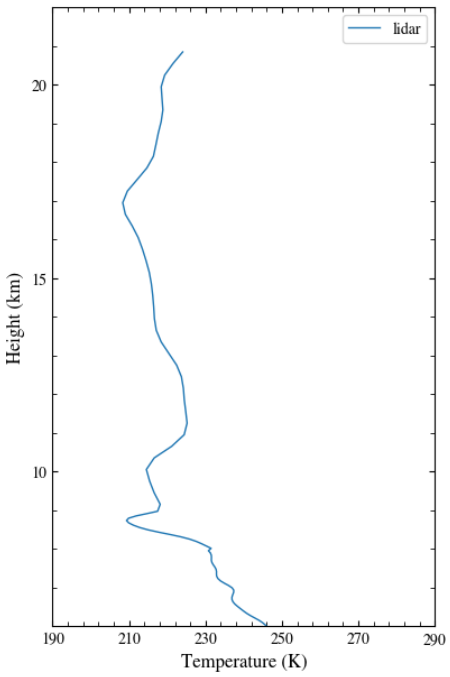


Figure R12. Atmospheric temperature profile retrieved from the lidar measurements under thin-cloud conditions, with a cloud layer located between approximately 8 and 9 km.

As shown in Fig. R12, the retrieved temperature profile exhibits noticeable discontinuities and deviations between 8 and 9 km, where the thin-cloud layer is located. These deviations are likely associated with the enhanced Mie scattering contribution within the cloud layer, which affects the reliability of the temperature retrieval. However, outside this altitude range, the retrieved temperature profile remains relatively continuous and smooth, without significant abrupt changes. This suggests that the influence of Mie scattering contamination on the retrieved temperature profile is primarily confined to the cloud layer, while the temperature retrievals at other altitudes remain relatively stable.

Comment 16)

Please explain if the measured instrument receiver's transmission spectrum measured in the laboratory setting is representative of the receiver transmission spectrum for field operation. Include any adjustments you apply to calibrations to account for the offsets, for example, in detector gain, laser pulse characterization, and indicate if you apply any

range dependent corrections to the receiver's transmission function.

Response:

Thank you for this valuable comment. Regarding the applicability of the laboratory-measured receiver transmission function to atmospheric observations, we would like to clarify that the receiver transmission function was characterized using both a 355 nm continuous-wave laser in the laboratory and the 355 nm pulsed laser employed in the actual lidar system.

Importantly, the pulsed-laser measurements were performed directly on the experimental lidar system. Furthermore, the optical fiber and fiber scrambler used during the calibration measurements were identical to those employed during the atmospheric observations. These arrangements helped minimize differences in optical illumination conditions between the calibration measurements and field operation.

Therefore, the receiver transmission function was characterized under optical conditions closely representative of those used during atmospheric measurements. We have further clarified these experimental arrangements in the revised manuscript (Page 15, Lines 320–325).

Regarding the detector gain correction, we have already addressed this issue in our response to Comment 11.

Regarding the characterization of the pulsed laser spectrum, the spectral response of the Fizeau interferometer was experimentally measured using the same pulsed laser employed during atmospheric measurements. Consequently, the measured spectral response inherently includes the broadening effect of the finite laser linewidth. By directly incorporating this experimentally measured response into the spectral retrieval model, the influence of the pulsed laser linewidth is already accounted for. Therefore, a separate measurement of the pulsed laser linewidth is not required for the retrieval process.

Regarding the laser center frequency, we actively stabilize it using a wavelength meter and monitor the laser wavelength in real time to minimize the impact of center-wavelength variations on wind velocity retrieval.

Regarding the range-dependent correction of the receiver transmission function, a

multimode optical fiber equipped with a mode scrambler was employed in our receiver system to improve the uniformity and stability of the illumination entering the Fizeau interferometer. The mode scrambler promotes mode coupling within the fiber, thereby reducing the sensitivity of the output intensity distribution to variations in the spatial and angular distributions of the atmospheric return signals at different altitudes. This configuration helps minimize range-dependent variations in the illumination conditions of the Fizeau interferometer. Therefore, a common experimentally characterized receiver spectral response was applied throughout the atmospheric retrieval, without introducing an additional range-dependent correction to the transmission function.

Comment 17)

Systematic Error budget: Please, provide an error budget estimate due to instrument hardware limitations: long term laser frequency locking accuracy and frequency drift, laser spectrum stability, interferometer drift, detector gain drift/after pulsing if relevant.

Response:

Thank you for this valuable comment. We appreciate the reviewer's suggestion to provide a more comprehensive assessment of the systematic uncertainties associated with the hardware performance of our lidar system. We agree that evaluating the influence of instrument stability and potential systematic errors is important for assessing the reliability of the retrieved atmospheric temperature and wind profiles. In response to this comment, we have further examined the relevant instrumental factors and provide detailed explanations below.

Regarding the laser frequency stability, we monitored the frequency fluctuations of the 355 nm pulsed laser using a HighFinesse WS8-2 wavelength meter. The measurement was conducted on 30 June 2026, and the results are presented in Fig. R9. The laser frequency remained relatively stable throughout the approximately 46-minute measurement period, without exhibiting a significant systematic drift. These results also demonstrate the effectiveness of the laser frequency-locking system in maintaining frequency stability during operation. The statistical distribution of the frequency fluctuations is shown in Fig. R9(b), with a standard deviation of 5.26 MHz which

corresponds to an equivalent line-of-sight velocity fluctuation of approximately 0.93 m s^{-1}. Importantly, during atmospheric observations, the transmitted laser frequency was continuously monitored using the wavelength meter, providing a real-time frequency reference for the Doppler wind retrieval. The recorded frequency variations can therefore be used to correct the frequency reference and reduce the influence of laser frequency fluctuations on the retrieved wind velocities. Furthermore, our lidar system determines the horizontal wind components from Doppler measurements performed in opposite viewing directions. By taking the difference between the Doppler velocities measured in opposite directions, common systematic frequency offsets can be largely cancelled, further reducing their influence on the retrieved wind profiles.

Regarding the laser spectral stability, before each atmospheric measurement, the spectral transmission response of the Fizeau interferometer was experimentally characterized using the same pulsed laser employed for atmospheric observations. The measured spectral response inherently includes the combined effects of variations in the laser spectral characteristics, potential drift of the Fizeau interferometer, and changes in the relative responses of individual channels of the linear PMT array. Therefore, comparing the spectral response curves obtained before different atmospheric measurements allows us to evaluate the overall stability of the receiver system. The corresponding experimental results are presented in Figure R13, showing good consistency among the independently measured spectral response curves. These results indicate that the combined effects of these potential instrumental variations were relatively small during the measurement periods.

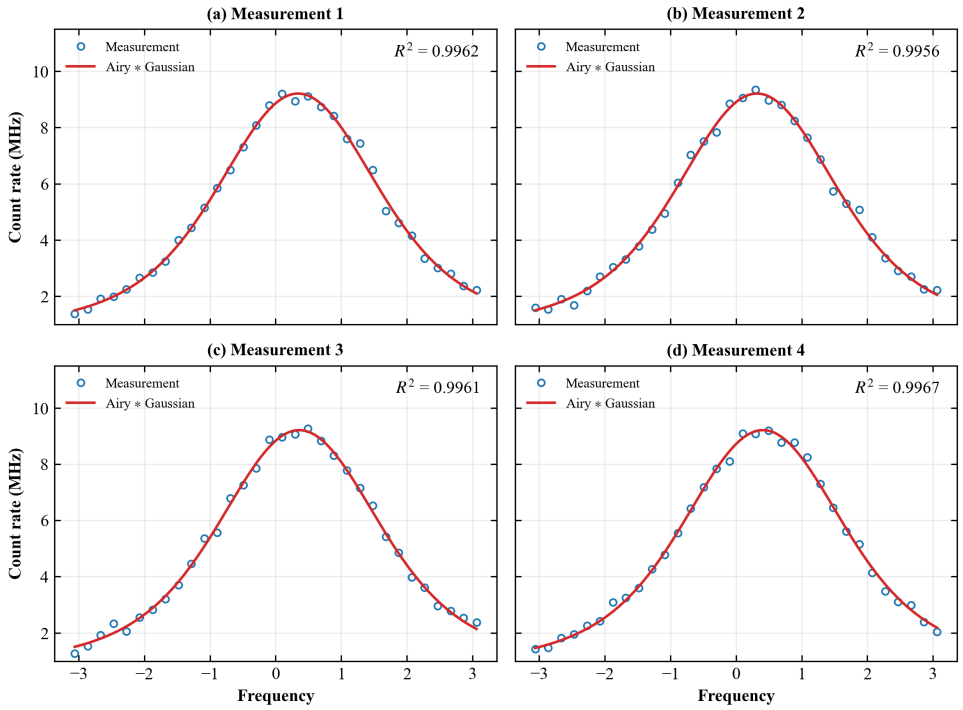


Figure R13. Receiver calibration results.

The four calibration measurements yielded a sample standard deviation of 12.3 MHz in the FWHM of the combined laser–Fizeau response, corresponding to approximately 0.40% of its mean spectral width. To assess the impact on temperature retrieval, the fitted responses were convolved with Rayleigh–Brillouin scattering spectra using the Witschas analytical model (Witschas, 2011a, b). For temperatures of 210–260 K and standard atmospheric pressures corresponding to altitudes of 2–20 km, the variability among these four calibrations produced a standard deviation of approximately 1.08–1.26 K in the retrieved temperatures.

Regarding the drift of the Fizeau interferometer, we analyzed the frequency-to-channel response to Doppler frequency shifts through six independent frequency-scanning calibration measurements. The mean calibration slope across the six measurements was 197.53 MHz/channel, with a relative slope variation (expressed as the relative standard deviation) of approximately 0.96%, indicating good repeatability of the Doppler frequency-shift response calibration under the tested conditions. The corresponding contribution to the wind-speed uncertainty is estimated to be approximately 0.19 m s^{-1} for a line-of-sight wind speed of 20 m s^{-1} (Pages 16, Lines 334–358). The added Fig. 9

is shown here as Fig. R14.

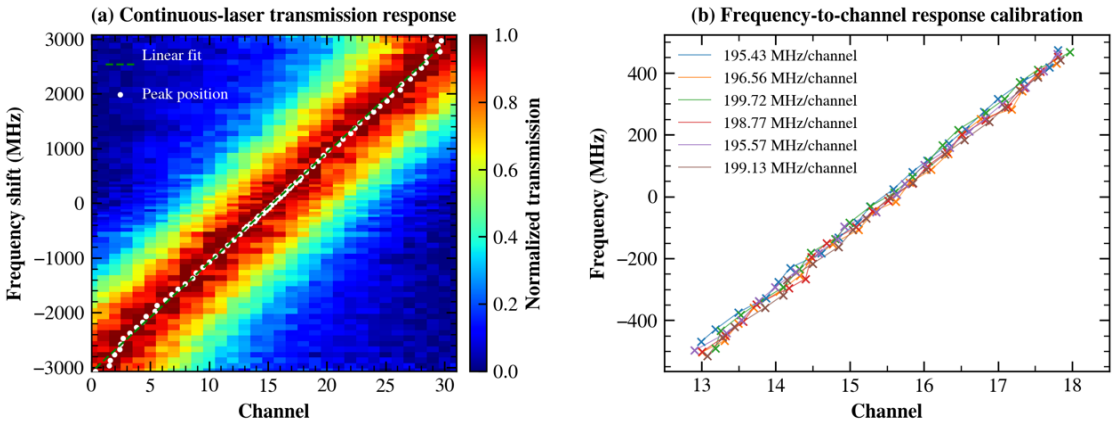


Figure R14. Calibration of the frequency-to-channel response. (a) Measured continuous-wave laser transmission response as a function of detector channel and laser frequency shift. The white dots indicate the fitted peak positions, and the dashed line represents the corresponding linear fit. (b) Frequency-to-channel response obtained from six independent frequency-scanning measurements, with the fitted slopes indicated in the legend.

Regarding the detector gain drift, the relative response differences among the 32 detector channels have been corrected using the illumination function. During atmospheric measurements, the photon-counting acquisition system operated with a dead time of 2 ns. To account for potential counting losses at high photon count rates, a dead-time correction can be applied to the measured photon counts based on the non-paralyzable detector model.

$$R_{corrected} = \frac{R_{measured}}{1 - R_{measured}\tau}$$

where $R_{corrected}$ represents the corrected photon count rate, $R_{measured}$ denotes the photon count rate recorded by the acquisition system, and τ is the dead time of the photon-counting system. This correction compensates for the underestimation of photon counts caused by the finite dead time of the acquisition system.

Furthermore, the receiver calibration inherently includes the combined effects of potential detector response drift, variations in the laser spectral characteristics, and drift of the Fizeau interferometer. Therefore, the influence of detector response variations is already reflected in the repeatability of the experimentally measured receiver response. The potential contribution of these combined instrumental variations to the wind-speed

uncertainty has been analyzed above.

The H11460-200 detector employs an ultra-bialkali (UBA) photocathode and a metal-channel dynode structure and is operated within the manufacturer's recommended operating limits. Förtsch et al. investigated 1100 Hamamatsu H12700 metal-channel multi-anode PMTs and reported a mean afterpulse probability of 0.93% (Förtsch et al., 2026). Dinoev et al. reported that Hamamatsu metal-channel photomultiplier tubes exhibited negligible signal-induced noise (SIN) under the right operating conditions (Dinoev et al., 2013). Therefore, we expect the influence of afterpulse on our lidar measurements to be relatively small and unlikely to represent a dominant source of retrieval uncertainty under our operating conditions.

Comment 18)

Indicate if the measurements can be performed during day time or are limited only to the night operation.

Response:

Thank you for this comment. At present, daytime measurements have not yet been conducted using our lidar system.

Comment 19)

Fig 2(a): The presented conceptual image lacks clear labeling, "faint" fiber connection. Please consider replacing this conceptual 3D image with a 2D optical schematics. Also, consider to use a presentation style similar to Xia et al., "Stratospheric temperature measurement with scanning Fabry-Perot interferometer for wind retrieval from mobile Rayleigh Doppler lidar," Optics Express, 22, 21775–21789 (2014). I believe this paper describes the same instrument.

Response:

Thank you for this valuable suggestion. We have revised Fig. 2 by replacing the original 3D optical layout with a clearer 2D optical schematic to better illustrate the optical configuration and light paths of the lidar system.

Comment 20)

Fig 2(b): The photograph appears to be not informative. I suggest replacing it with 2D schematics of the Fizeau optical layout or use a semitransparent 3D CAD rendering. Please use font colors with higher contrast for labels.

Response:

Thank you for this valuable suggestion. We have retained the original photograph in Fig. 2(b) and added a 3D CAD schematic of the receiver to provide a clearer illustration of its internal optical configuration and component arrangement. In addition, we have used higher-contrast font colors for the labels to improve their visibility and readability.

Comment 21)

Fig 2(c): The photograph is not informative and appears to show a black shipping container. Please consider replacing it with an image of the actual instrument or semitransparent 3D CAD rendering.

Response:

Thank you for this valuable suggestion. We have replaced the original photograph of the USTC Doppler wind lidar in Fig. 2(c) with a 3D rendering to provide a clearer and more informative representation of the instrument's overall structure. The revised Fig. 2 is shown here as Fig. R15.

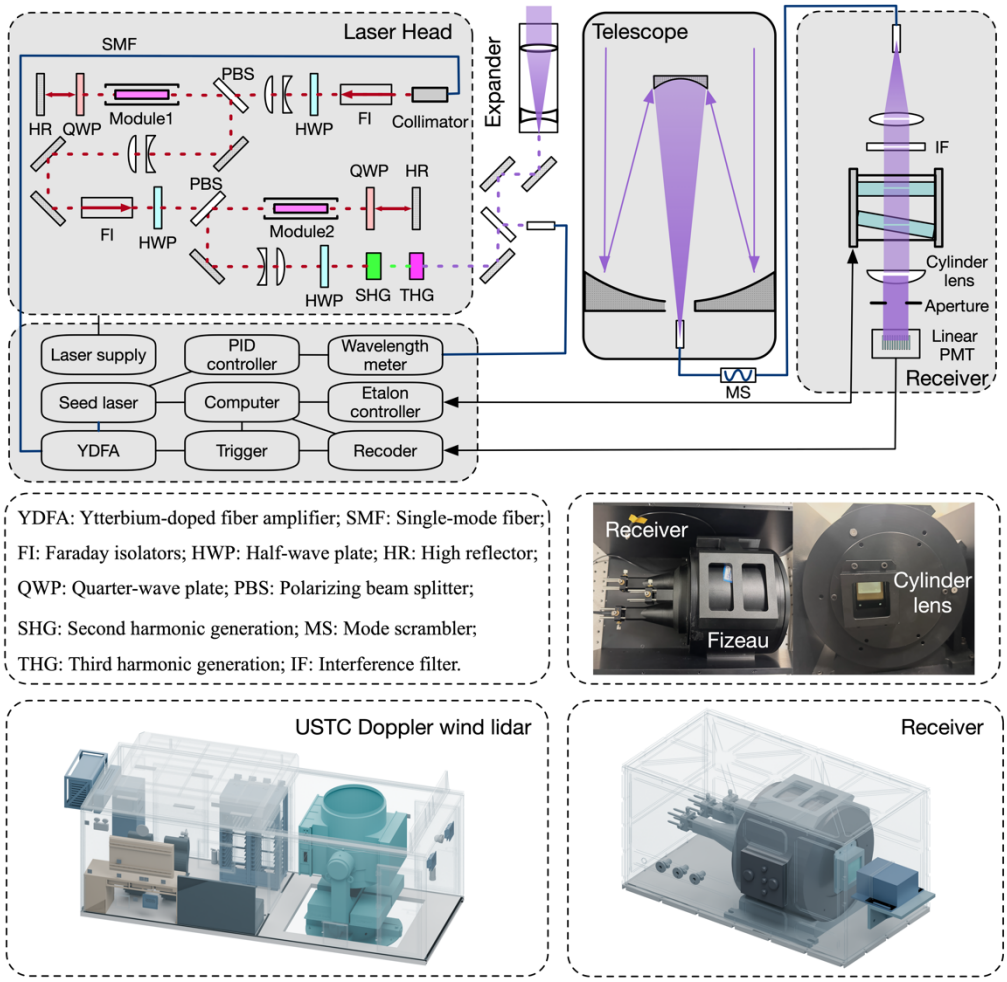


Figure R15. Schematic of the developed HSRL system.

Comment 22)

Line 193: Please replace “fineness” with “finesse” throughout the manuscript, including the tables.

Response:

Thank you for pointing out this terminology error. We have replaced "fineness" with "finesse" as suggested. The corresponding corrections have been made on Page 5, Line 143.

Comment 23)

Line 320: Please replace “Mie scattering energy” with “Mie scattering signal” for consistency with the terminology.

Response:

Thank you for pointing out this terminology issue. We have replaced "Mie scattering energy" with "Mie scattering signal" in the revised manuscript, as suggested by the reviewer. The corresponding corrections have been made on Page 1, Lines 24; Page 4, Line 117; and Page 18, Line 370**.**

Comment 24)

Throughout the manuscript: The authors report simulated temperature and wind retrieval error with two decimal places. This may be confused with the measurement accuracy of the instrument. Please reconsider how you report the results of these simulations to make it consistent with the error estimates.

Response:

Thank you for this valuable suggestion. We have revised the numerical precision of the simulated temperature and wind retrieval errors throughout the manuscript to avoid confusion with the actual measurement accuracy of the lidar system.

References in this response:

Dinoev, T., Simeonov, V., Arshinov, Y., Bobrovnikov, S., Ristori, P., Calpini, B., Parlange, M., and van den Bergh, H.: Raman Lidar for Meteorological Observations, RALMO – Part 1: Instrument description, Atmospheric Measurement Techniques, 6, 1329-1346, 10.5194/amt-6-1329-2013, 2013.

Förtsch, J., Kampert, K. H., Patel, V., Pauly, C., and Pfeifer, D.: Series testing and characterization of 1100 Hamamatsu H12700 Multianode Photomultiplier tubes, Nuclear Instruments and Methods in Physics Research Section A: Accelerators, Spectrometers, Detectors and Associated Equipment, 1083, 171147, https://doi.org/10.1016/j.nima.2025.171147, 2026.

Hagen, N., Kupinski, M., and Dereniak, E. L.: Gaussian profile estimation in one dimension, Applied Optics, 46, 5374-5383, 10.1364/AO.46.005374, 2007.

Witschas, B.: Analytical model for Rayleigh–Brillouin line shapes in air, Applied Optics, 50, 267-270, 10.1364/AO.50.000267, 2011a.

Witschas, B.: Analytical model for Rayleigh–Brillouin line shapes in air: errata, Applied Optics, 50, 5758-5758, 10.1364/AO.50.005758, 2011b.